Radiative convective equilibrium over a land surface

Nicolas Rochetin
Columbia University
New York, NY 10027

Benjamin R. Lintner
Rutgers, the State University of New Jersey
New Brunswick, NJ 08901

Kirsten L. Findell
Geophysical Fluid Dynamics Laboratory
Princeton, NJ 08542

Adam H. Sobel
Columbia University
New York, NY 10027

Pierre Gentine[1]
Columbia University
New York, NY 10027

[1] Corresponding author: Pierre Gentine, Earth Institute / Department of Earth and Environmental Engineering, Columbia University, 500 W 120th St., New York, NY 10027, email: pg2328@columbia.edu

Abstract

Radiative-convective equilibrium (RCE) describes an idealized state of the atmosphere in which the vertical temperature profile is determined by a balance between radiative and convective fluxes. While RCE has been applied extensively over oceans, its application over the land surface has been limited. The present study explores the properties of RCE over land using an atmospheric single column model (SCM) from the Laboratoire de Meteorologie Dynamique (LMD) General Circulation Model (LMDZ5B) coupled in temperature and moisture to a land surface model comprising a simplified bucket model with finite moisture capacity. Given the presence of a large-amplitude diurnal heat flux cycle, the resultant RCE exhibits multiple equilibria when conditions are neither strictly water- nor energy-limited. By varying top-of-the-atmosphere insolation (through changes in latitude), total system water content, and initial temperature conditions, the sensitivity of the land RCE states is assessed, with particular emphasis on the role of clouds. Based on this analysis, it appears that a necessary condition for the model to exhibit multiple equilibria is the presence of low-level clouds coupled to the diurnal cycle of radiation. In addition the simulated surface precipitation rate varies non-monotonically with latitude as a result of a tradeoff between in-cloud rain rate and subcloud rain re-evaporation, thus underscoring the importance of subcloud layer processes and unsaturated downdrafts. It is shown that clouds, especially at low levels, are key elements of the internal variability of the coupled land-atmosphere system through their feedback on radiation.

1. Introduction

The concept of radiative-convective equilibrium (RCE) was introduced by Manabe and Wetherald (1967), following the earlier work of Gold (1909) and Goody (1949), to describe an idealized, statistical state of the atmosphere in which a balance between radiative cooling and convective heating determines the vertical temperature profile. RCE postulates that, on average, convective scale motions compensate for the destabilization of the atmosphere by radiation. RCE represents a powerful tool for estimating convective sensitivity to ocean surface temperature and for diagnosing the possible mechanisms through which deep convection is maintained and interacts with the surface fluxes in the absence of large-scale flow. RCE has been applied to a wide range of problems, including estimation and scaling of convective mass fluxes (Tompkins and Craig 1998a), the organization of tropical deep convection (Tompkins and Craig 1998b, Tompkins 2001a,b) and climate sensitivity to greenhouse gas forcing (Muller et al. 2011; Romps 2011).

In most of the applications of RCE in either single column models (SCMs) or cloud resolving models (CRMs), the surface boundary has been an ocean, often with prescribed surface temperature. Complications over land stem from the greater complexity associated with interacting components such as vegetation, soil moisture, and soil temperature. However, some studies have simplified the land system to address these complications. For instance, RCE has been considered for a swamp surface (Manabe and Wetherald 1967; Renno 1997) or with a constrained hydrologic cycle (i.e. with prescribed evapotranspiration) and nudging of 10 cm soil temperature toward a prescribed value (Prigent et al., 2011). Tompkins and Craig (1998a) and

69 Schlemmer et al. (2011) performed an experiment involving a CRM coupled to land
70 surface in which the system achieves a ”diurnal equilibrium” state, i.e. a quasi-stationary
71 regime in which the surface and the boundary layer temperatures exhibit diurnal
72 oscillations. In these studies, the soil and atmospheric temperature profiles were
73 relaxed toward climatological values at points far from the surface.

74 In our study, we consider an extension of the concept of RCE applied to a land
75 surface with a closed (water-conserving) hydrologic budget. As far as we are aware,
76 ours is the first study to evaluate equilibrium land-atmosphere coupling in an SCM fully
77 coupled to a land surface model. Of particular interest in our exploration of RCE over
78 land is the potential existence of multiple equilibria. For prescribed-SST conditions, the
79 RCE state is uniquely determined by the SST and radiative forcing, i.e., in the absence
80 of energy exchange through the surface (and associated advective transport), the
81 isolated, fixed SST RCE system possesses a unique equilibrium solution (Hilbert 1912;
82 Tompkins and Craig 1998b; Renno 1997), with the ocean acting as both a thermostat
83 and an infinite water source. On the other hand, Renno (1997) and Tompkins (2001a,b)
84 showed that introduction of a surface hydrologic cycle through a swamp ocean, in which
85 the surface temperature is interactively determined through the balance of surface
86 fluxes assuming zero soil heat capacity, permits the existence of multiple equilibria.
87 Even if multiple equilibria are not realized in the real climate system, e.g., because of
88 the presence of internal variability or seasonal evolution, they may nonetheless provide
89 insights regarding the evolution of the coupled land-atmosphere system.

90 Over land the existence of multiple equilibria has been explored in the context of
91 land-atmosphere feedbacks. For instance, large-scale continental recycling forced by

92 stochastic advection exhibits two distinct equilibria comprising dry and moist surface
93 states (Rodríguez-Iturbe et al. 1991a,b; Entekhabi et al. 1992). Land and boundary-
94 layer interactions can also induce bimodality in the surface Bowen ratio (Entekhabi and
95 Brubaker 1995; Brubaker and Entekhabi 1995). Similarly, Wang and Eltahir (2000)
96 demonstrated the emergence of multiple equilibria in simulations of the West African
97 climate including biosphere-atmosphere interactions. The Global Land Atmosphere
98 Coupling Experiment (GLACE; Koster et al. 2004) suggests the existence of land-
99 atmosphere coupling hotspots, which typically occur in the transition zones between
100 arid and humid regions. The physical mechanisms that produce such hotspots are still
101 not completely understood, although some progress has been made using some
102 simplified analysis of the land surface coupled to the atmosphere (e.g. Guo et al. 2006;
103 Koster et al. 2006; DelSole et al. 2009, Lintner et al. 2013). Recently, Aleina et al.
104 (2013) demonstrated the emergence of multiple equilibria (desert or forest) for a toy
105 model of a planet when interactive vegetation is included.
106 Apart from the GCM-based analyses of GLACE, most studies of the feedbacks of
107 soil moisture and precipitation over land have been performed over relatively short time
108 scales from one to several days (Hohenegger et al. 2009; Seneviratne et al. 2010;
109 Gentine et al. 2013), or by aggregating diurnal-scale processes over the summer
110 season (D'Odorico and Porporato 2004; Findell et al. 2011). A key challenge for the
111 analysis of observations and complex GCMs is that weather and climate variability may
112 overwhelm or otherwise mask signatures of land-atmosphere coupling (Phillips and
113 Klein 2014). Thus, we believe that analyses performed using idealized frameworks such
114 as the model considered here can stimulate improved understanding of long-term

(seasonal, annual) land-atmosphere interactions: what such analyses may lack in terms of realism is leveraged against the ease and transparency of diagnosis.

The paper is structured as follows. Section 2 provides an overview of the Laboratoire de Meteorologie Dynamique (LMD) General Circulation Model (LMDZ5B) SCM used in this study and the experimental setup employed to obtain RCE solutions over land. In section 3, we document the existence of multiple equilibria in a set of experiments in which we vary latitude, total (soil plus atmosphere) moisture content, and initial soil temperature, while Section 4 provides a more in-depth analysis of the RCE solutions and how these relate to land surface, cloud-radiative, and convective processes in the model. In section 5, we present the results of sensitivity experiments to assess how the diurnal cycle of radiation and cloud radiative feedbacks impact the existence of multiple equilibria. The final section summarizes the key findings of this study and discusses some implications of land region RCE for interpreting land region climate.

2. Model description and setup:

2.1. Model description:

2.1.1. Atmosphere

We use the SCM version of the LMDZ5B GCM developed by the Laboratoire de Meteorologie Dynamique (Hourdin et al. 2012). LMDZ5B has been used to perform climate simulations for the IPCC 5th assessment report. Here we give a brief description of the model; the reader is referred to Hourdin et al. (2012) for a more extensive discussion.

The model has 39 nonuniformly-spaced levels in the vertical. The first grid point is at 35 m, with 8 grid-points distributed in the first kilometer. Between 1 and 20 km, the mean vertical resolution is 800 m and the model top is located at 40 km. Separate parameterizations of shallow and deep convection are included. For shallow convection, the eddy diffusive scheme of Mellor and Yamada (1994) is combined with a mass-flux representation of boundary-layer thermals (Hourdin et al. 2002; Rio and Hourdin 2008; Rio et al. 2010) to account for, respectively, turbulence in the surface and inversion layers, and non-local convective transport induced by boundary layer coherent structures. Thermals are represented using a bulk entraining-detraining plume approach (Simpson and Wiggert 1969; Betts 1973) to compute the properties of a mean characteristic thermal representing the dry and cloudy (if saturation level is reached) boundary-layer thermals present in a model grid-cell. The plume model diagnoses the heights of cumulus base and top, as well as the vertical profiles of the plume vertical velocity, thermodynamic properties and fractional coverage, through the vertical evolution of mass flux.

Emanuel's deep convection scheme (Emanuel 1991) is added to this scheme for the treatment of precipitating-deep convection. The scheme has been modified by Grandpeix and Phillips (2004) to improve the sensitivity of the simulated deep convection to tropospheric relative humidity (Derbyshire et al. 2004). The triggering criterion of deep convection is based on the concept of available lifting energy (*ALE*) provided by boundary-layer thermals: deep convection is triggered whenever *ALE* overcomes the convective inhibition (*CIN*). A cold pool (or wake) parameterization has also been added to Emanuel's scheme with cold pools fed by the unsaturated

160 downdrafts resulting from rain re-evaporation (Betts 1976; Tompkins 2001b) outside the
161 cloud. These cold pools also provide updraft lifting energy that may re-trigger deep
162 convection by exceeding the *CIN* (Tompkins 2001b). The closure follows Grandpeix and
163 Lafore (2010) and relates the cloud-base mass flux to the available lifting power (*ALP*)
164 provided by subcloud processes, *CIN*, and the vertical velocity at the level of free
165 convection (see details in Grandpeix et al. 2010; Grandpeix and Lafore 2010).

166 In the LMDZ GCM, precipitation is divided into (1) a convective part, generated
167 by Emanuel's convection scheme (i.e. cumulonimbus clouds); and a (2) stratiform part,
168 generated by (i) large-scale condensation related to a grid-scale ascent, (ii) boundary-
169 layer thermal plumes related to cumulus clouds and (iii) turbulent diffusion related to
170 fog. However since there is no large-scale ascent in the present RCE SCM framework,
171 clouds and precipitation are completely determined by the parameterized subgrid-scale
172 processes, i.e. turbulence, shallow convection and deep convection. The radiation
173 scheme (Morcrette 1991) fully interacts with clouds and other components of the
174 atmosphere. In LMDZ5B, maximum cloud overlapping is applied to compute radiative
175 forcing when adjacent layers are cloudy, as for cumulus clouds, whereas the random
176 overlapping is applied when two cloudy layers are separated by at least one clear layer,
177 as for stratiform clouds.

178 For both stratiform and convective clouds, cloud cover is computed following a
179 statistical cloud scheme with a log-normal probability density function, representing the
180 subgrid-scale variability of total water content (Bony and Emanuel 2001). In this
181 scheme, the in-cloud water content q_{inc}, condensed water q_c and cloud fraction are
182 deduced from the distribution and average saturation of specific humidity. In the current

183 standard version of LMDZ5B, ice thermodynamics is not taken into account in the deep
184 convection scheme. Inclusion of ice increases the cold pool intensity and thereby
185 strengthens deep convection via the *ALP* closure, although this has been found to have
186 little effect on upper level heating rates.

187 ### 2.1.2. Soil Model

188 The soil model uses a diffusion scheme for heat propagation, assuming a
189 diffusivity of 1.06 x 10^{-6} m^2 s^{-1}. A zero ground heat flux condition is imposed at infinite
190 depth. The dynamics of soil water content Q_{soil} is represented with a simple bucket
191 model (Manabe, 1969, Koster and Suarez 1994), and includes precipitation,
192 evaporation and runoff generation. A soil saturation threshold is prescribed at Q_{max}
193 =1.5m, above which the excess of water is removed completely via runoff. Under these
194 conditions, total water content of the land-atmosphere system, $Q_{tot} = Q_{soil} + W$, where
195 W is precipitable water, is no longer conserved. However, in our experiments, Q_{max} is set
196 to a sufficiently large value (1.5m) to avoid runoff and therefore non-conservation.
197 Physically Q_{max} corresponds to an effective rooting depth (Rodríguez-Iturbe et al. 1999;
198 Laio et al. 2001) although the model contains no explicit representation of vegetation.
199 The surface albedo is taken as α=0.19. Although this highly reduced soil model may
200 affect the coupling between the soil and the atmosphere, we show below that the
201 simplified system still permits nonlinearities and multiple equilibria.

202 ### 2.1.3. Surface Fluxes

203 Sensible heat flux and evaporation are computed via bulk formulations:
204 $\phi_{\text{sens}} = \rho V_0 C_{d,v} C_{d,h} (T_s - T_1)$ and $Evap = \beta E_{\text{pot}}$ with E_{pot} the potential evaporation computed

as $E_{\text{pot}} = \rho V_0 C_{d,v} C_{d,h} (q_{sat,T_s} - q_1)$ and β the evapotranspiration coefficient reflecting linear soil moisture stress. Here, ρ=1.17 kg/m^3 is the surface air density, V_0 is the first level wind speed, $C_{d,v}$ the neutral drag coefficient for a land surface, $C_{d,h}$ the stability correction based on the local Richardson number (see Hourdin et al. 2012), C_p=1004 J K^{-1} kg^{-1} is the dry air heat capacity, T_s the surface skin temperature, T_1 the first atmospheric layer temperature, q_{sat,T_s} the saturation specific humidity at the surface, and q_1 the first layer specific humidity. β varies linearly between 0 and 1 for soil moisture content between Q_{soil} and $Q_{max}/2$ and saturates at β=1 for $Q_{soil} > Q_{max}/2$. This relationship actually mimics idealized vegetation, for which stomatal opening depends quasi-linearly on soil moisture up to a maximum value (saturation) (Porporato et al. 2001). If $Q_{soil} > Q_{max}$, runoff is generated to maintain $Q_{soil} = Q_{max}$ (see previous subsection).

2.2. Methodology:

The LMDZ5B SCM is integrated for 10 years with a time step Δt = 450 s, LMDZ standard time step used for CMIP5 simulations. An initial atmospheric profile (extracted from the First ISCCP Regional Experiment - FIRE - campaign, see Cox *et al*. 1987) is prescribed, as well as initial, vertically uniform, ground temperature T_0 and soil moisture Q_0. The RCE framework is applied without large-scale velocity or tendencies, as in most prior studies of oceanic RCE. A diurnal cycle of incoming solar radiation is imposed at TOA, corresponding to the annual mean value at the prescribed latitude. The model computes a residual surface wind, driven by convective-scale motions, that maintains consistent surface fluxes. Over oceanic surfaces, some surface wind must be included

to ensure heat and moisture transfer; indeed, surface wind provides the mechanical forcing (forced convection) that critically contributes to surface fluxes over oceans. Over land, however, daytime heating of the surface provides surface buoyancy instability (free convection) that thermally drives surface energy exchanges. Thus, surface wind is much less critical over lands than over the ocean. In section 5, we perform a sensitivity analysis on the impact of relaxing the atmosphere toward a nonzero geostrophic wind and found that it does not modify the conclusions reached here.

The sensitivity experiments discussed in the following sections consider changes in (i) latitude, λ; (ii) total water content, Q_{tot}; and (iii) initial ground temperature, T_0. Note that variation of total water content is performed by varying the initial soil water content Q_0 while maintaining the same initial precipitable water W_0 = 25 kg/m².

2.3. Characteristics of the baseline LMDZ5B RCE state:

We run the model for the following baseline conditions: λ=35°, T_0=300K, Q_{tot} = 40 mm (i.e. Q_0 = 15 mm). When the soil-atmosphere system reaches TOA radiative equilibrium, a diurnal-mean equilibrium surface temperature is reached. The system may require several years to achieve equilibrium because of the large soil depth and its corresponding thermal inertia. In this study, we assume that 10 years is a sufficiently long period for the soil to approximately equilibrate with the atmosphere, i.e. with an imbalance inferior to 4 W/m².

The atmosphere is in RCE when the net atmospheric radiative cooling balances the net convective heating. In fact, an atmospheric equilibrium is reached within a few weeks (see Fig 1a) and thereafter holds throughout most of the simulation. Indeed, the daily-averaged time series of the radiative cooling (Q_{rad}) and convective heating (Q_{con})

profile nearly balance each other. The time scale of convection (few hours) is much shorter than the radiative time scale (around 40 days), so any fluctuation in the surface energy or TOA radiation budgets is rapidly eliminated by convection (Cronin and Emanuel, 2013). Consequently, on daily timescales the integrated atmospheric energy budget is zero in all simulations at equilibrium, as depicted by the solid line in Fig 1b. In other words, RCE guarantees the same net energy flux at the surface and at TOA since there is no energy accumulation in the atmosphere. Consequently, the dashed line in Fig 1b not only represents the net energy flux but also the net energy flux at TOA. Periods where the two curves are superimposed in Fig 1b correspond to periods where the atmospheric energy loss (gain) corresponds to a similar energy gain (loss) for the soil. However, because of its large depth, the soil requires some time to balance atmospheric perturbations and the whole soil-atmosphere system may not be at equilibrium. For example, in simulation year 1984, the atmosphere experiences a strong perturbation that induces a departure from the preceding RCE state. This large atmospheric fluctuation drives a soil response at longer timescales through a surface temperature increase (see Fig 1c). Again before the final stable RCE is reached, the entire land-atmosphere system may be out of equilibrium as the soil column adjusts. In this unstable regime, the inherent system internal variability can generate jumps from one equilibrium state to another one. Hence, the system can pass through different equilibria states before reaching its final steady RCE solution. Hereafter, we only consider the RCE state reached after 10 years of simulation (assuming it is close enough to the final RCE).

Fig 2 depicts the diurnal course of energy fluxes for the control run (CTL). The bucket soil model (bucket) used in the LMDZ5B SCM may be compared with a slab ocean model with a small heat capacity, which allows diurnal variations in surface temperature, but with a larger Bowen ratio and limited water holding capacity. Because of the small thermal soil inertia the system oscillates around the equilibrium state on daily timescales (see Fig 2a).

As already seen in Fig 1, the surface and TOA energy budgets are close to zero in the baseline simulation. The RCE over a land surface reaches a steady periodic regime, in which the diurnal solar forcing drives a periodic response of the land-atmosphere system, both in terms of surface temperature and precipitation as seen in Fig 2a and Fig 2b. At equilibrium, surface temperature and precipitation exhibit very little day-to-day variability (not shown). The diurnal cycle of T_s exhibits a 1- to 2-hour lag with respect to solar forcing, which is characteristic of land surfaces for which the maximum is typically reached between 1300 LT and 1600 LT (Gentine et al. 2010). Regarding precipitation, prior studies have documented the presence of an afternoon peak in land region precipitation, especially in the tropics, in observations and CRMs (e.g. Bechtold et al. 2004; Guichard et al. 2004; Dai 2006; Rio et al. 2009, 2012). Thus, the land region RCE in the LMDZ5B SCM produces consistent diurnal cycle phasing relative to observations and high-resolution models.

After 10 years of simulation, RCE applies to daily averages. Fig 2c demonstrates that the subdaily (hourly) behavior deviates from RCE. The maximum soil heating occurs early in the morning, when turbulent fluxes are relatively weak and cannot dissipate much of the radiative input; rather, most of the heating at this time is

295 dissipated as ground heat flux (Gentine et al. 2011; 2012). In terms of hydrologic cycle,
296 the daily-averaged precipitation and evaporation balance each other with surface
297 precipitation rates across the suite of simulations ranging from one to three
298 mm/day (discussed below).

299 Fig 2d depicts the diurnal evolution of radiative and convective heating integrated
300 over the atmospheric column. Convective heating exhibits a strong diurnal cycle
301 imposed by the large-amplitude diurnal variations in surface turbulent heat fluxes. The
302 net radiative energy budget of the atmosphere is positive between 9 and 15 LT because
303 of the large shortwave absorption. Diurnal variations in longwave tendencies are an
304 order of magnitude smaller than the shortwave ones. Continental RCE is thus achieved
305 for daily averages: the atmosphere experiences a net heating during daylight hours
306 compensated by an equivalent net cooling at night. This is a key difference with a
307 prescribed-SST framework over the ocean, in which the fixed SST ensures a permanent
308 energy balance (i.e. verified at each instant), with continuous precipitation. The large
309 diurnal cycle over land surfaces, induced by the low continental heat capacity compared
310 to the ocean, provides increased surface variability compared to the oceanic case with
311 prescribed SST. Even at equilibrium there can be substantial subdiurnal changes in
312 surface temperature, boundary layer depth, cloud cover, and convection, which can
313 respond nonlinearly to the diurnal course of radiation. This added variability appears to
314 play a role in determining the equilibrium states (Rodriguez-Iturbe et al. 1991), as will be
315 seen in section 5. The addition of the surface hydrological cycle, which limits the
316 amount of available water at the surface, also increases the system's degrees of
317 freedom compared to the prescribed-SST RCE. The energy in the system is thus

318 controlled by the latitude (and prescribed planetary albedo), and the hydrologic cycle is
319 constrained by the initial total water content Q_0.

320 3. Existence of multiple equilibria

321 The sensitivity of RCE to changes in solar forcing, total moisture and initial
322 surface temperature is investigated by modifying three parameters: the latitude λ, the
323 total water content Q_{tot}, through specification of initial soil water content Q_0, and initial
324 ground temperature T_0. Each pair of latitude and total water contents may be viewed as
325 distinct climatological conditions. λ ranges from 30° to 40° in increments of 2.5°. As we
326 will see in the following, this range is sufficient to cover the entire spectrum of possible
327 RCE states. The initial Q_0 ranges from 5 mm to 45 mm in increments of 10 mm, or
328 equivalently, Q_{tot} , ranges from 30 mm to 70 mm. For each of the 25 climate states, the
329 LMDZ5B SCM is initialized with one of 5 values of T_0 ranging from 280 K to 320 K with
330 an increment of 10 K, giving a total of 125, 10-year simulations. Note that all other
331 model parameters are set to the baseline values. In what follows, we describe each
332 simulation's final state by its mean equilibrium surface temperature (K) and soil water
333 content (mm). For some latitude and total water content pairs, distinct final states are
334 obtained with different initial ground temperatures. Thus, the coupled soil-atmosphere
335 system exhibits multiple equilibria (see next section).

336 Fig. 3 provides an overview of the RCE combinations for the different λ, T_0, and
337 Q_0. Before discussing the sensitivity analysis, we point out that a strong negative
338 correlation exists between equilibrium soil surface temperature T_s and soil moisture
339 content Q_{soil}. In the simplified bucket land surface hydrology the evapotranspiration

efficiency β increases linearly with soil moisture (see section 2.1.2.). Low Q_{soil} generates low evaporation, so most of the net radiative heating at the surface must be balanced by sensible heat flux (or ground heat flux). On the other hand, latent heat release is a more efficient heat transfer mechanism than other heat fluxes at medium to high temperature (Bateni and Entekhabi 2012). For low soil moisture, surface temperature quickly rises since the available cooling mechanisms are not efficient. Such behavior is well known for the daily variations of surface skin temperature and is used as an indicator of water stress (Bastiaanssen et al. 1998; Castelli et al. 1999; Boulet et al. 2007).

No multiple equilibria are seen at either high (λ = 40°) or low (λ = 30°) latitudes. For these latitudes, the RCE is either "warm and dry surface" (see Fig 3 red symbols) or "cool and wet surface" (Fig 3 blue symbols). The warm-dry RCE corresponds to a high surface temperature associated with a nearly dry soil (Q_{soil} < 5 mm), while the cool-wet RCE corresponds to a low surface temperature associated with a high soil water content and low precipitable water (W ~ 5 mm). The warm and cool RCE equilibria can be found at all latitudes and total water contents. In other words, for any latitude and total water content, there is at least one T_0 that can lead to a warm-dry or a cool-wet solution. However, the warm-dry and cool-wet solutions can exhibit different surface temperatures depending on the solar forcing and water availability.

As seen in Figure 4 as an example, for Q_0 = 5 mm (i.e. Q_{tot} = 30mm) increasing latitude (i) favors cool solutions and (ii) leads to a monotonic decrease of final soil temperature for both warm and cool solutions. Moreover, the sensitivity of the equilibrium solution to a change in latitude is more pronounced for warm solutions. Indeed, the final T_s ranges from 274 K to 278 K for the cool states, whereas it ranges

363 from 296 K to 306 K for the warm solutions. Sensitivity to Q_0 is nontrivial: at the extreme
364 latitudes, the warm RCE state (λ = 30°) is dependent on total available moisture while
365 the cool state (λ = 40°) is not. From Fig 3a, it is clear that the warm states become
366 warmer with increasing Q_{tot} at low latitudes. At 30° (Fig 3a), T_s increases from 306 K to
367 316 K with Q_{tot} increasing from 30 to 70 mm. However, at high latitudes (see Fig 3e) T_s
368 decreases from 274 K to 272 K with Q_{tot} increasing from 30 mm to 70 mm. Thus, at 30°
369 the final state is "water-limited": incoming radiation is large and generates large surface
370 evaporation so that the soil is effectively desiccated. Increasing Q_{tot} similarly increases
371 precipitable water, which in turn leads to a strong water vapor greenhouse effect
372 causing T_s to increase. At high latitudes (λ = 40°) nearly all available water in the
373 system resides in the soil, leaving the atmosphere nearly devoid of moisture. This
374 corresponds to an "energy-limited" regime: TOA incoming insolation is insufficient to
375 generate substantial surface evaporation (or latent heat release). However, since β is
376 an increasing function of Q_{soil}, Q_{soil} increases evaporation, which ultimately increases
377 precipitable water. Under cold conditions, the humidity profile is very close to saturation;
378 hence, even a small increase of precipitable water induces more low-level clouds, which
379 reduces incoming surface shortwave radiation and results in a (small) decrease of T_s.
380 To summarize, the sensitivity of RCE states to changes in total water content is:
381 (i) of opposing sign for high and low latitudes, and (ii) of larger magnitude at low
382 latitudes. Such differential sensitivity can be explained through distinct responses of the
383 atmospheric radiative properties to changes in precipitable water. Low incoming
384 radiation induces cold conditions and high relative humidity, which strengthens low-level

cloud cover and cloud optical thickness. High incoming radiation induces warm conditions associated with increased precipitable water.

Apart from the extreme latitudes, intermediate solutions (Fig 3 green symbols) and multiple equilibria are found to occur at all other latitudes considered (see Fig 3b,c and d). These intermediate RCE states are associated with water being more equitably partitioned between the soil and the atmosphere (Q_{soil} > 5 mm and W > 5 mm). In these experiments, the multiple equilibria appear to be either bimodal or trimodal. For intermediate latitudes, there is an optimum range of Q_{tot} that favors multimodal solutions and the intermediate RCE states. Fig 3 shows that, for Q_{tot} = 30 mm (i.e Q_0 = 5 mm), it is not possible to reach an intermediate RCE state for any of the latitudes considered (i.e., green symbols are absent). Only warm and cool equilibria are present for intermediate latitudes. Low values of Q_{tot} appear to favor bimodality (warm and cool states) rather than multimodality (warm, intermediate and cool). At large total water content, Q_{tot} = 70 mm, the multiple equilibria disappear (see Fig 3d), as the model tends to a cool RCE state regardless of the initial condition. In conclusion, we note here an "optimum" range of λ (energy) and Q_{tot} (water) values that allow intermediate states with neither a completely dry, desert-like, nor fully wet, swamp-like, surface. This range corresponds to a regime that is neither "energy-limited" (in terms of solar radiation) nor "water-limited" (in terms of total water content). Within this range, the coupled land-atmosphere SCM system exhibits multimodal RCE states.

4. Investigation of equilibria states (dry, wet and intermediate): Sensitivity to latitude and the role of clouds

4.1. Diagnosis of RCE state dependence on latitude:

To understand the characteristics of the RCE states, including the genesis of multiple equilibria, we consider here how the system evolves toward these states at different latitudes. To do so, we focus on the simulations with Q_{tot} = 60 mm and T_0 = 280K. From Fig 3, we note that this set of conditions gives the range of RCE states—warm, cool and intermediate—over 30° to 40°.

Fig 5 depicts 10-day moving averages of the time series of surface temperature, soil water content, precipitation and precipitable water at each latitude. For all latitudes except *30°* these variables reach a steady state after ~1 year. On the other hand, for λ = *30°* there is a transient regime comparable to the one observed in Fig 1. The coupled land-atmosphere system exhibits large, quasi-periodic, oscillations at the monthly time scale (rather than the single big jump observed in Fig 1a) during the first half of the simulation and then smoothly converges towards its stable solution. The coupled land-atmosphere system is capable of producing internal variability that can cause transitions from one equilibrium state to another one. Fig 5 also shows that the nontrivial latitude dependence of these variables. The warm (λ =30°) and cool solutions (λ = 37.5° and 40°) are clearly distinguishable, whereas the two intermediate RCE states (λ = 32.5° and λ = 35°) are quite close to each other, with equilibrium surface temperatures of 297.5 K and 295 K for λ = 32.5° and λ = 35°, respectively.

The (surface) precipitation rate provides an indication of the intensity of the hydrologic cycle at equilibrium: it is equal to the surface evapotranspiration when RCE is reached. The latitude dependence of surface precipitation is not only nonlinear but also non-monotonic, as it increases from a minimum value λ = 30° (1.2 mm/day) to a

peak value at λ = 32.5° (~2.85 mm/day) and then decreases toward higher latitudes. In the next subsection, we present and discuss mean vertical profiles at equilibrium to elucidate the behavior of precipitation with latitude.

4.2. Mean Vertical profiles:

Mean vertical profiles of heating tendencies, relative humidity, and precipitation averaged over the last three months of the simulation are depicted in Fig 6. The heating tendencies (Fig 6a) elucidate some important characteristics of the RCE states, including the strength and depth of convection. RCE is found to hold at essentially every point in the vertical, as, on average, turbulent diffusion, shallow and deep convection heating compensates radiative cooling at each level. It is interesting to point out that some RCE solutions manifest similar column-integrated tendencies but with very different vertical heating profiles. Consequently, a continental RCE state is better defined by its surface temperature and soil moisture (or precipitable water) state, rather than by its column-integrated radiative cooling (or convective heating). According to Fig 6a, the principal differences in the radiative heating vertical distribution among the different equilibria, and thus in the convective heating profiles, are readily seen in the vertical extent of the radiative convective instability, with both convection height and strength decreasing with latitude. For the cool-wet and warm-dry cases, the respective convection heights are ~ 300 hPa and ~ 150 hPa. This result is consistent with the monotonic decrease of the average surface temperature with latitude, which exerts a strong control on convection depth via control of the moist adiabatic temperature profile (Larsson & Hartmann, 2005). Larsson and Hartmann (2005) argue that the altitude at

452 which radiative cooling drops to zero determines the anvil top, i.e. the cloud top
453 detrainment zone.

454 Apart from the overall profile vertical extent, the largest heating tendency
455 differences across the latitude range occur around the 750 hPa level and near the
456 surface. At 37.5° and 40°, a peak in net radiative cooling is present at 600 hPa and is
457 associated with net radiative heating immediately below. This radiative heating dipole is
458 not present at the other latitudes. For λ = 35° and 37.5°, intense radiative cooling
459 occurs in the lowermost atmospheric layer. In subsection 4.3, we demonstrate that
460 these features in the radiative heating profiles are related to the vertical distribution of
461 cloudiness.

462 The mean vertical profiles of relative humidity (Fig 6b) and precipitation (Fig 6c)
463 are also useful for distinguishing RCE states, as they clearly show daily-mean boundary
464 layer depth, cloud top, and levels of rainfall generation and re-evaporation. Starting from
465 the surface, the first peak in relative humidity indicates the daily-mean boundary layer
466 depth, or the daily-mean cloud base, while the second peak indicates the daily-mean
467 cloud top. At λ = 30°, the boundary layer is significantly drier and higher than in other
468 cases because of both the large surface sensible heat flux and boundary layer top dry
469 air entrainment. Rain re-evaporation in the subcloud layer is, in turn, dramatically
470 increased (Fig 6c, red curve). Consideration of the vertical profiles of precipitation points
471 to the source of the maximum surface rain simulated λ = 32.5°. In particular, the vertical
472 structure suggests a tradeoff between convection maximum strength and rain re-
473 evaporation beneath cloud base. With increasing insolation, the vertical profile of
474 convective heating shifts upward and strengthens. Thus, the maximum rain rate rises

475 monotonically from ~ 1.7 mm/day at 750 hPa for λ = 40° to ~ 4.7 mm/day at 600 hPa
476 for λ = 30 ° (see Fig 6c). On the other hand, rain re-evaporation increases as the cloud
477 base rises. Thus, for the warmest case, the rain rate decreases from 4.7 mm/day at 600
478 hPa to 1.2 mm/day at the surface. In summary, convection strengthens as latitude
479 decreases but boundary layer deepening and drying enhances evaporative cooling in
480 the lower atmosphere. This strong evaporative cooling fuels very intense unsaturated
481 downdrafts that spread at the surface as density currents (not shown).

482 In the cool cases (λ = 37.5° and λ = 40°) relative humidity is larger although there
483 is much less precipitable water than in other cases (see Fig 5). From the surface to the
484 cumulonimbus top, relative humidity always exceeds 50% because the atmosphere is
485 so cold that the partial pressure of saturation is low. Intermediate solutions (λ = 32.5°
486 and λ = 35°) exhibit very similar vertical profiles of relative humidity and precipitation,
487 with little difference in the convection depth.

488 The three families of continental RCE states thus exhibit very distinct vertical
489 profiles. Each one of the preferred states seems to correspond to a particular vertical
490 structure of the atmosphere. The next subsection investigates the role of clouds in the
491 establishment of these three families of solutions.

492 **4.3. Cloud cover**

493 The mean diurnal cycle of the vertical distribution of cloud fraction at equilibrium
494 are displayed in Fig 7. Total cloud cover, especially low-level cloud over, increases with
495 latitude. Oppositely, cloud top decreases with latitude, in agreement with the decreasing
496 vertical extent of moist convection. During the daytime, cloud amount is also maximized

497 because of moist convection. More importantly, cloud fractions clearly reveal the 3
498 different RCE types: warm, intermediate and cool.

499 In the warm case (λ = 30°, Fig 7a) cloud amount is low. Cumulus cloud base
500 rises from 800 hPa to 700 hPa from 1000 LT to 1400 LT, while cumulonimbus cloud top
501 is located around 150 hPa and exhibits the strongest cloud fraction between 1300 LT
502 and 1800 LT. In the LMDZ5B SCM, cumulus clouds are located at the detrainment zone
503 of moist thermal plumes originating from the surface. When triggered, deep convection
504 generates deep cumulonimbus that transports heat and moisture from the lower free
505 troposphere to its top. In the model, the sudden disappearance of shallow cumuli
506 synchronized with deep convection initiation is due to precipitation. Indeed, once deep
507 convection is triggered, heavy rainfall and associated cold pools fed by unsaturated
508 downdrafts tend to cool and stabilize the boundary layer (Tompkins 2001a,b; Grandpeix
509 et al. 2010; Grandpeix and Lafore 2010). This stabilization likely accounts for the
510 sudden disappearance of low-level clouds in the mid-afternoon, despite the fact that
511 convective precipitation is still present. Then, the time lag between low- and high-level
512 clouds illustrates the succession between shallow and deep convective regimes in all
513 cases listed in Fig 7. However, we point to the shorter duration of convective events in
514 the warm cases. In summary, two successive cloud layers characterize the warm RCE
515 states: a cumulus layer followed by a cirrus layer collocated with the cumulonimbus
516 cloud detrainment zone. They exert a net positive radiative forcing in the underlying
517 atmosphere and at the surface (Bony et al. 2004; Bony and Dufresne 2005; Bony et al.
518 2006). We shall notice the absence of mid-level clouds. This lack of mid-level clouds is

519 a long-standing issue in LMDZ as in many GCMs, which is related to the
520 misrepresentation of congestus clouds.

521 Intermediate states (λ =32.5° and λ =35°, Fig 7b and 7c) are characterized by the
522 presence of three distinct cloud layers: (i) a high one at the anvil top, (ii) a low one,
523 which corresponds to the development of a shallow cumulus layer prior to deep
524 convective onset, and (iii) a third one just above the surface that corresponds to
525 morning fog occurring between 0300 LT and 0900 LT. This foggy layer represents a
526 distinct behavior from an oceanic boundary, since it is generated by rapid nocturnal
527 cooling of the surface, which leads to the a low condensation point observed in Fig 6a
528 (yellow and green curves) near the surface. This condensed layer is thus mostly
529 induced by the diurnal evolution of the land surface energy budget and especially by its
530 nighttime cooling, unlike stratocumuli over the ocean, which are induced by a
531 combination of surface latent heat flux, a shallow boundary layer, and large-scale
532 subsidence. This condensed layer plays a very important role in cooling the lower
533 atmosphere by reflecting incoming sunlight. The layer delays sunlight surface heating
534 and the morning deepening of the boundary layer, thereby modulating the entire diurnal
535 cycle of convection. We shall notice that the absence of surface wind in our experiments
536 favors the development and persistence of morning fog. In section 5 we evaluate the
537 effect of wind on the RCE. At about 0900 LT, the fog disappears and shallow convection
538 starts. Associated cumulus clouds develop until the deep convective onset, at around
539 1500 LT. Deep convection activity lasts for about 6 hours.

540 For cool RCE states (i.e. λ =37.5° and 40°, Fig 7d and 7e), the succession of
541 shallow and deep regimes is less obvious. A permanent stratocumulus layer is present

542 at 750 hPa, which cools the lower atmosphere and strongly limits cumulus and
543 cumulonimbus development. In the LMDZ5B SCM, this permanent cloud layer is
544 collocated with turbulent motions associated with strong destabilization generated by
545 cloud top radiative cooling. Indeed, this cloud layer is nearly opaque to both incoming
546 shortwave radiation and outgoing longwave radiation (Wood 2012), explaining the
547 strong radiative cooling peak near cloud top (750 hPa) observed in Fig 6a (light blue
548 and blue curves). This dense cloud layer also traps longwave radiation in the lower
549 atmosphere, leading to net radiative heating around 850 hPa (see Figure 5a). The
550 second peak is located much higher, between 500 hPa and 250 hPa, and corresponds
551 to the anvil cloud top. However, the cirrus radiative feedback is not sufficient to balance
552 the strong surface cooling induced by the permanent stratocumulus layer.

553 In summary, in the cool RCE state, the atmosphere is so cold that the low
554 saturation partial pressure is associated with large relative humidity values. The high
555 relative humidity in turn favors the presence of a permanent low-level cloud layer, which
556 is nearly opaque to daytime shortwave radiation heating of the surface and ultimately
557 maintains the system in a cold state. The system is then locked into a very stable
558 regime. Analogous stable, cold, and cloudy states have been found in other studies
559 using SCMs such as the CFMIP-GASS Intercomparison of LES and SCM models
560 (CGILS) (Zhang et al. 2012), which sought to enhance understanding of the transition
561 from stratocumulus to cumulus regimes. Brient (2011) found that adding stochastic
562 noise to the vertical motion field greatly improves an SCM's capacity to mimic the
563 observed cloud cover vertical distribution. This suggests that maintaining a constant
564 vertical wind velocity, as is the case here may favor "locked" cloudy regimes in SCMs.

4.4. Summary:

To summarize the results, we have shown that the coupled land-atmosphere system supports multiple RCE states and can exhibit multiple equilibria based on the initial temperature of the system. The final equilibrium states fall into three main categories: i) cool and wet surface, ii) warm and dry surface, and ii) intermediate temperature and moisture regimes. Each state corresponds to a stable cloud regime. Clouds and their interaction with radiation are suspected to play a key role in the establishment and maintenance of these equilibrium states. Each type of RCE corresponds to a certain vertical and temporal distribution of cloudiness: a 2- layer (daytime cumulus and evening cirrus) configuration for warm RCEs, a 3-layer configuration (morning fog, daytime cumulus and evening cirrus) for intermediate RCEs, and a 3-layer configuration (permanent stratocumulus, daytime cumulus and evening cirrus) for cool RCEs. This result holds true for the 125 experiments conducted in section 3.

5. Role of cloud radiative feedback on multiple equilibria

The relative importance of clouds for the emergence of multiple equilibria is now evaluated. A sensitivity experiment for the range of T_0 and Q_{tot} values at λ=35° was performed without cloud radiative forcing, i.e. clouds were rendered transparent to both shortwave and longwave radiation. The RCE states for these sensitivity experiments are plotted in Fig 8. Removing the cloud radiative forcing eliminates multiple equilibria, at least for the conditions considered here. Moreover, none of the final states exhibits a warm-dry or a cool-wet RCE, rather, all final states are grouped around T_s = 300 K and

587 water is present in both the soil and atmosphere, as with the intermediate RCE states
588 described above. Hence, Fig 8 strongly supports the hypothesis that cloud radiative
589 forcing is a necessary condition for the presence of multiple equilibria. The continental
590 RCE framework allows a diurnal cycle of surface temperature that naturally introduces
591 some variability into the system. For instance, the presence of morning fog is
592 determined by the minimum nighttime surface temperature. Hence, if an internal
593 perturbation results in a drop in the minimum nocturnal temperature, the morning fog
594 may appear and delay the surface and atmospheric heating, increasing the probability
595 of obtaining a colder surface on the following day. Ultimately, the system may fall into a
596 colder equilibrium. Such a feedback loop involving clouds and radiation is rendered
597 possible by the presence of the large diurnal variations of surface temperature. In the
598 following, we attempt to identify the main cloud types contributing to the simulated
599 nonlinearities and multiple equilibria.

600 We reproduce the sensitivity to latitude experiment conducted in Section 4 under
601 four different configurations, in order to quantify the relative role of low (i.e. below 600
602 hPa) and high (i.e over 600 hPa) clouds. The original (fully coupled clouds) experiment
603 is compared with three other experiments in which: (i) all clouds are transparent to
604 radiation (see Fig 9b: “no clouds” experiment); (ii) only low clouds interact with radiation
605 (see Fig 9c: “low clouds only” experiment); and (iii) only high clouds interact with
606 radiation (see Fig 9d: “high clouds only” experiment). Since the “no-cloud” (Fig 9b) and
607 “high-cloud only” (Fig 9d) experiments exhibit similar behaviors, we conclude that high-
608 clouds are not a leading-order source of nonlinearity. Indeed, the equilibrium surface
609 temperature decreases linearly with latitude when only the high cloud radiative forcing is

610 retained (see Fig 9d). Compared to the “no-cloud” experiment (Fig 9b), high clouds
611 significantly heat the atmosphere and the surface through their longwave greenhouse
612 effect. Without the cloud radiative effect, equilibrium surface temperatures ranges from
613 289 to 308K, whereas inclusion of high-cloud radiative forcing increases this range from
614 292 to 313K.

615 When only low-cloud radiative forcing is included, the system may be attracted
616 toward multiple preferred states, similar to what was observed in Figs 5 and 9a.
617 Therefore we conclude that, within the LMDZ5B SCM, low-level clouds are the main
618 source of nonlinearity leading to multiple equilibria. Low-level clouds are already known
619 to be a principal source of GCM spread (Bony et al. 2004; Bony and Dufresne 2005;
620 Bony et al. 2006); here their importance is further emphasized over land regions
621 through the prism of the RCE framework. Of course, since LMDZ5B SCM tends to
622 underestimate mid-level clouds, as do many GCMs, this conclusion should be viewed
623 with caution. Indeed, undersimulation of mid-level clouds may exaggerate the role of
624 low-level clouds.

625 Overall, these results underscore clouds as a critical component of the land-
626 atmosphere system’s nonlinearity, with the diurnal cycle enhancing the internal
627 variability that allows the presence of multiple equilibria. In the presence of interactive
628 clouds, the RCE states correspond to distinct cloud vertical distributions as depicted in
629 Figure 7. Feedback pathways associated with convection, clouds and radiative cooling,
630 may favor some convective regimes over others. That is, clouds strongly modulate the
631 radiative cooling profiles with which the convective heating profiles must adjust to obtain

RCE. In turn, vertical mixing of heat and moisture induced by moist convection ultimately leads to cloud formation, which affects radiation.

We performed similar experiments with an SCM based on the version of the LMDZ GCM used for the 4th IPCC assessment (AR4) (Hourdin 2006) to check the model-dependency of the results (not shown). In this version, multiple equilibria were less common in the 30° to 40° range of latitudes, and fewer low clouds were observed in these simulations as well. Indeed, Hourdin (2006) pointed out that an important bias of the AR4 version of the LMDZ GCM was its inability to represent low-level cumulus and stratocumulus. The absence of parameterization for coherent boundary layer structures (thermals) in this model version likely accounts for the lack of simulated cumulus clouds. At first glance, these results imply that low-level clouds are necessary for obtaining multiple equilibria, although additional analysis are required to substantiate this.

It is reasonable to consider how much the results presented here may depend on the details of the model configuration or the assumptions. Clearly, a comparison of multiple models would be useful in addressing some concerns about model dependence. Although a complete assessment regarding how model configuration or assumptions impact the results is beyond the scope of the current study, we reproduced the 125 experiments listed in section 3 with a wind forcing nudged toward a geostrophic value of 10 m/s, in order to study the effect of large-scale forcing on the final equilibrium of the system. The wind profile computation results from the interaction between horizontal wind and surface roughness, turbulence and thermals. Hence, we introduce an additional feedback loop into the system: the wind fully interacts with the SCM

boundary layer parameterizations (but not deep convection). The resulting wind profile is constant in the free troposphere (V = 10 m/s) and mimics the Ekman spiral in the boundary layer, with a parabolic decrease of the wind magnitude resulting in a surface wind V_0 ~ 0.7 m/s.

Fig 10 is the equivalent of Fig 8 with a geostrophic wind forcing. The main conclusion is that multiple equilibria still exist as long as cloud radiative feedback is retained. However the number of final equilibria is slightly reduced and the final states are distinct from the equilibria obtained without wind. In particular, the morning fog disappears because of the added mechanical forcing which increases surface exchange and boundary layer entrainment. The disappearance of fog in turn reduces the vertical degrees of freedom in the cloud distribution and therefore the number of final RCE states. When clouds are made transparent to radiation, the multiple equilibria again disappear, similar to the model behavior in the absence of geostrophic wind. Thus, the interaction between the geostrophic wind and boundary layer processes does not diminish the importance of clouds, and especially their radiative feedback, as the main source of internal variability. Finally, comparing Fig 8b with Fig 10b in the absence of cloud radiative feedback, we observe that the RCE states are very close whether or not geostrophic wind is present. Indeed, the unique final equilibrium temperature is nearly 300 K in all cases, while soil water content is increased by ~ 5 mm with geostrophic wind forcing. This strongly suggests that wind influences the final states via cloud formation. In other words, when clouds are transparent to radiation, the wind stress does not considerably change the results, and more generally the wind-boundary layer feedback becomes of secondary importance. Overall, this experiment further supports

678 the key role of cloud-radiation interactions in generating internal variability in the
679 coupled soil-atmosphere system.

680 6. Summary and conclusions

681 In this study we have examined the applicability of RCE over a land surface
682 using a single column atmosphere version of the LMDZ GCM coupled to an idealized
683 land surface model. Relative to its oceanic counterpart, the land system has a finite
684 moisture capacity corresponding to the total water content in the soil and in the
685 atmosphere since atmospheric transport and runoff are assumed to be zero, i.e. the
686 hydrologic cycle is locally closed. Over the ranges of latitude and total water content
687 explored, multiple equilibria can be obtained by varying initial soil temperature. Three
688 classes of final RCE states are possible, namely: i) a hot state with a hot and dry
689 surface and most of the system water content residing in the atmosphere; ii) an
690 intermediate state with water partitioned between the soil and in the atmosphere; and iii)
691 a cold state with a wet surface and nearly no moisture present in the atmosphere.

692 By considering sensitivity experiments in which boundary layer diurnal cycle and
693 cloud radiative forcing are disabled, we show how these are necessary for the
694 occurrence of multiple equilibria in the LMDZ5B SCM and how they determine the
695 characteristics of the final RCE states. In particular, low-level clouds and fog appear to
696 play a key role in the presence of multiple equilibria. For low total water content
697 conditions, the system is bimodal, while increasing total water content allows the
698 emergence of the RCE states with water in both the soil and atmosphere. These
699 intermediate states correspond to either two- or three-layer cloud fraction distributions.

In two-layer state, the succession of shallow and deep convection during daytime leads to cumulus and anvil clouds. In the three-layer state, morning fog develops before shallow convection onset. Above a threshold value for total water content multiple equilibria are no longer supported, and the system falls into a cold state. High relative humidity then favors the presence of a permanent, thick layer of low-level clouds. Outside of the latitude range emphasized here (30º-40º), all water evaporates from the surface (low latitude hot states), corresponding to a water-limited regime, or precipitates (high latitude cold states), corresponding to an energy-limited regime.

For a model configuration in which low-level clouds are rendered transparent to radiation, the multiple equilibria disappear, which emphasize the key role of clouds and of their radiative feedbacks in the land-atmosphere system. Overall our results of the radiative convective equilibrium over land indicate that the cloud radiative feedback, interacting with the diurnal cycle of radiation, induces bifurcations in the land-atmosphere system and therefore determines the equilibrium conditions in the land-atmosphere system.

Acknowledgements

BRL and PG acknowledge funding support from NSF-AGS 1035843, PG acknowledges support from DOE-ASR DE-SC0008720, and AHS acknowledges support from NSF AGS-1008847. The authors thank Gilles Bellon, Christoph Schär and Bjorn Stevens for stimulating discussions of this work and three anonymous reviewers for their careful reading and comments.

REFERENCES:

Aleina, F. C., M. Baudena, F. D'Andrea, and A. Provenzale, 2013: Multiple equilibria on planet Dune: climate–vegetation dynamics on a sandy planet. *Tellus B*, **65**, 693, doi:10.1029/2006RG000217.

Bastiaanssen, W. G. M., M. Menenti, R. A. Feddes, and A. A. M. Holtslag, 1998: A remote sensing surface energy balance algorithm for land (SEBAL) - 1. Formulation. *J Hydrol*, **212-213**, 198–212, doi:10.1016/S0022-1694(98)00253-4.

Bateni, S. M., and D. Entekhabi, 2012: Relative efficiency of land surface energy balance components. *Water Resour Res*, **48**, W04510–, doi:10.1029/2011WR011357.

Bechtold, P., J. Chaboureau, A. Beljaars, A. K. Betts, M. Kohler, M. J. Miller, and J. Redelsperger, 2004: The simulation of the diurnal cycle of convective precipitation over land in a global model. *Q J Roy Meteor Soc*, **130**, 3119–3137, doi:10.1256/qj.03.103.

Betts, A. K., 1973: Non-precipitating cumulus convection and its parameterization. *Q J Roy Meteor Soc*, **99**, 178–196.

Betts, A. K., 1976: The Thermodynamic Transformation of the Tropical Subcloud Layer by Precipitation and Downdrafts. *Journal of Atmospheric Sciences*, **33**, 1008–1020, doi:10.1175/1520-0469.

Bony, S. and Coauthors, 2006: How well do we understand and evaluate climate change feedback processes? *J Climate*, **19**, 3445–3482.

Bony, S., and J. Dufresne, 2005: Marine boundary layer clouds at the heart of tropical cloud feedback uncertainties in climate models. *Geophys Res Lett*, **32**, L20806, doi:10.1029/2005GL023851.

Bony, S., and K. A. Emanuel, 2001: A parameterization of the cloudiness associated with cumulus convection; Evaluation using TOGA COARE data. *J Atmos Sci*, **58**, 3158–3183.

Bony, S., J. L. Dufresne, H. Le Treut, J. J. Morcrette, and C. Senior, 2004: On dynamic and thermodynamic components of cloud changes. *Clim Dynam*, **22**, 71–86, doi:10.1007/s00382-003-0369-6.

Boulet, G., Chehbouni, A., Gentine, P., Duchemin, B., Ezzahar, J., & Hadria, R. 2007: Monitoring water stress using time series of observed to unstressed surface temperature difference. *Agricultural and Forest Meteorology*, ***146***, 159–172. doi:10.1016/j.agrformet.2007.05.012

Brubaker, K., and D. Entekhabi, 1995: An analytic approach to modeling land atmosphere interaction 1. Construct and equilibrium behavior. *Water Resour Res*, **31**, 619–632.

757 Castelli, F., D. Entekhabi, and E. Caporali, 1999: Estimation of surface heat flux and an
758 index of soil moisture using adjoint-state surface energy balance. *Water Resour Res*,
759 **35**, 3115–3125.

760 Cox, S.K., Mc Dougal, D. S., Randall, D. A. and Schiffer, R. A., 1987: FIRE: the First ISCCP
761 Regional Experiment. *Bulletin of the American Meteorological Society*, **68**, 114-118

762 Cronin, T. W., & Emanuel, K. A. 2013: The climate time scale in the approach to radiative-
763 convective equilibrium. *J. Adv. Model. Earth Syst*, (in press). doi:10.1002/jame.20049

764 Dai, A., 2006: Precipitation characteristics in eighteen coupled climate models. *J Climate*,
765 **19**, 4605–4630.

766 DelSole, T., M. Zhao, and P. A. Dirmeyer, 2009: A New Method for Exploring Coupled
767 Land-Atmosphere Dynamics. *J Hydrometeorol*, **10**, 1040–1050,
768 doi:10.1175/2009JHM1071.1.

769 Derbyshire, S., I. Beau, P. Bechtold, J. Grandpeix, J. Piriou, J. Redelsperger, and P. M. M.
770 Soares, 2004: Sensitivity of moist convection to environmental humidity. *Q J Roy*
771 *Meteor Soc*, **130**, 3055–3079, doi:10.1256/qj.03.130.

772 Emanuel, K. A., 1991: A Scheme for Representing Cumulus Convection in Large-Scale
773 Models. *J Atmos Sci*, **48**, 2313–2335.

774 Entekhabi, D., and K. Brubaker, 1995: An analytic approach to modeling land-atmosphere
775 interaction, 2, Stochastic formulation. *Water Resour Res*, **31**, 633–643.

776 Entekhabi, D., I. Rodríguez-Iturbe, and R. L. Bras, 1992: Variability in Large-Scale Water-
777 Balance with Land Surface Atmosphere Interaction. *J Climate*, **5**, 798–813.

778 Findell, K., P. Gentine, and B. Lintner, 2011: Probability of afternoon precipitation in eastern
779 United States and Mexico enhanced by high evaporation. *Nat Geosci*, **4**, 434–439,
780 doi:10.1038/NGEO1174.

781 Gentine, P., A. A. M. Holtslag, F. D'Andrea, and M. Ek, 2013: Surface and atmospheric
782 controls on the onset of moist convection over land. *J Hydrometeorol*,
783 130211131121003, doi:10.1175/JHM-D-12-0137.1.

784 Gentine, P., B. Heusinkveld, and D. Entekhabi, 2012: Systematic Errors in Ground Heat
785 Flux Estimation and Their Correction. *Water Resour Res*, **48**, W09541,
786 doi:10.1029/2010WR010203.

787 Gentine, P., D. Entekhabi, and J. Polcher, 2010: Spectral Behaviour of a Coupled Land-
788 Surface and Boundary-Layer System. *Bound-Lay Meteorol*, **134**, 157–180,
789 doi:10.1007/s10546-009-9433-z.

790 Gentine, P., J. Polcher, and D. Entekhabi, 2011: Harmonic propagation of variability in
791 surface energy balance within a coupled soil-vegetation-atmosphere system. *Water*
792 *resources Research*, **47**, –, doi:10.1029/2010WR009268.

793 Gold, E., 1909. The isothermal layer of the atmosphere and atmospheric radiation.
794 *Proceedings of the Royal Society of London. Series A*, ***82***(551), 43-70.
795
796 Goody, R. M., 1949. The thermal equilibrium at the tropopause and the temperature of
797 the lower stratosphere. *Proceedings of the Royal Society of London. Series A.*
798 *Mathematical and Physical Sciences*, ***197***(1051), 487-505.
799
800 Grandpeix, J. Y., and V. Phillips, 2004: Improved Mixing Representation in Emanuel's
801 Convection Scheme. *Q J Roy Meteor Soc*, **130**, 3207–3222, doi:10.1256/qj.03.144.

802 Grandpeix, J.-Y., and J.-P. Lafore, 2010: A Density Current Parameterization Coupled with
803 Emanuel's Convection Scheme. Part I: The Models. *J Atmos Sci*, **67**, 881–897,
804 doi:10.1175/2009JAS3044.1.

805 Grandpeix, J.-Y., J.-P. Lafore, and F. Cheruy, 2010: A Density Current Parameterization
806 Coupled with Emanuel's Convection Scheme. Part II: 1D Simulations. *J Atmos Sci*, **67**,
807 898–922, doi:10.1175/2009JAS3045.1.

808 Guichard, F. and Coauthors, 2004: Modelling the diurnal cycle of deep precipitating
809 convection over land with cloud-resolving models and single-column models. *Q J Roy*
810 *Meteor Soc*, **130**, 3139–3172, doi:10.1256/qj.03.145.

811 Guo, Z. and Coauthors, 2006: GLACE: The Global Land-Atmosphere Coupling Experiment.
812 Part II: Analysis. *J Hydrometeorol*, **7**, 611–625.

813 Hilbert, D., 1912: Bergrundung der elementaren Strahlungstheorie, *Physik Zeitschrift*, **13**,
814 1056-1064

815 Hohenegger, C., P. Brockhaus, C. S. Bretherton, and C. Schaer, 2009: The Soil Moisture-
816 Precipitation Feedback in Simulations with Explicit and Parameterized Convection. *J*
817 *Climate*, **22**, 5003–5020, doi:10.1175/2009JCLI2604.1.

818 Hourdin, F., F. Couvreux, and L. Menut, 2002: Parameterization of the dry convective
819 boundary layer based on a mass flux representation of thermals. *J Atmos Sci*, **59**,
820 1105–1123.

821 Hourdin, F., J. Y. Grandpeix, C. Rio, S. Bony, and A. Jam, 2012: LMDZ5B: the Atmospheric
822 Component of the IPSL Climate Model with Revisited Parameterizations for Clouds and
823 Convection. *Clim Dynam*, doi:10.1007/s00382-012-1343-y.

824 Koster, R. D. and Coauthors, 2006: GLACE: The Global Land-Atmosphere Coupling
825 Experiment. Part I: Overview. *J Hydrometeorol*, **7**, 590–610.

826 Koster, R. D., and M. J. Suarez, 1994: The Components of a Svat Scheme and Their
827 Effects on a Gcms Hydrological Cycle. Vol. 17 of, Advances in Water Resources, 61–
828 78.

829 Laio, F., A. Porporato, L. Ridolfi, and I. Rodríguez-Iturbe, 2001: Plants in water-controlled
830 ecosystems: active role in hydrologic processes and response to water stress - II.
831 Probabilistic soil moisture dynamics. *Adv Water Resour*, **24**, 707–723.

832 Lintner, B.R., P. Gentine, K.L. Findell, F. D'Andrea, A.H. Sobel, and G.D. Salvucci, 2013:
833 An idealized prototype for large-scale land-atmosphere coupling. *J. Clim.*, **26**, 2379—
834 2389, doi:10.1175/JCLI-D-11-000561.1

835 Manabe, S., and R. T. Wetherald, 1967: Thermal equilibrium of the atmosphere with a given
836 distribution of relative humidity. *The Warming Papers: The Scientific Foundation for the*
837 *Climate Change Forecast*, 94–115.

838 Manabe, S., 1969: Climate and ocean circulation 1: The atmospheric circulation and the
839 hydrology of the Earth's surface. *Mon. Weather Rev.*, **97**, 739-774

840 Muller, C. J., P. A. O'Gorman, and L. E. Back, 2011: Intensification of Precipitation
841 Extremes with Warming in a Cloud-Resolving Model. *J Climate*, **24**, 2784–2800,
842 doi:10.1175/2011JCLI3876.1.

843 Phillips, T. J., & Klein, S. A. 2014. Land-atmosphere coupling manifested in warm-season
844 observations on the US southern great plains. *Journal of Geophysical Research:*
845 *Atmospheres (In press)*.
846 Porporato, A., F. Laio, L. Ridolfi, and I. Rodríguez-Iturbe, 2001: Plants in water-controlled
847 ecosystems: active role in hydrologic processes and response to water stress - III.
848 Vegetation water stress. *Adv Water Resour*, **24**, 725–744.

849 Prigent, C., Rochetin, N., Aires, F., Defer, E., Grandpeix, J-Y., Jimenez, C., and Papa, F.,
850 2011: Impact of the inundation occurence on the deep convection at continental scale
851 from satellite observations and modeling experiments. *Journal of the Geophysical*
852 *Research, Atmosphere*, **116**, D24

853 Renno, N., 1997: Multiple equilibria in radiative-convective atmospheres. *Tellus Series A-*
854 *Dynamic Meteorology And Oceanography*, **49**, 423–438.

855 Rio, C., and F. Hourdin, 2008: A thermal plume model for the convective boundary layer:
856 Representation of cumulus clouds. *J Atmos Sci*, **65**, 407–425,
857 doi:10.1175/2007JAS2256.1.

858 Rio, C., F. Hourdin, F. Couvreux, and A. Jam, 2010: Resolved Versus Parametrized
859 Boundary-Layer Plumes. Part II: Continuous Formulations of Mixing Rates for Mass-
860 Flux Schemes. *Bound-Lay Meteorol*, **135**, 469–483, doi:10.1007/s10546-010-9478-z.

861 Rio, C., F. Hourdin, J. Y. Grandpeix, and J. P. Lafore, 2009: Shifting the diurnal cycle of
862 parameterized deep convection over land. *Geophys Res Lett*, **36**, –,
863 doi:10.1029/2008GL036779.

864 Rio, C., J. Y. Grandpeix, F. Hourdin, and F. Guichard, 2012: Control of deep convection by
865 sub-cloud lifting processes: the ALP closure in the LMDZ5B general circulation model.
866 *Clim Dynam*, 2271–2292.

867 Rodríguez-Iturbe, I., A. Porporato, L. Ridolfi, V. Isham, and D. R. Cox, 1999: Probabilistic
868 modelling of water balance at a point: the role of climate, soil and vegetation. *P R Soc*
869 *A*, **455**, 3789–3805.

870 Rodríguez-Iturbe, I., D. Entekhabi, and R. L. Bras, 1991a: Nonlinear Dynamics of Soil-
871 Moisture at Climate Scales .1. Stochastic-Analysis. *Water resources Research*, **27**,
872 1899–1906.

873 Rodríguez-Iturbe, I., D. Entekhabi, J. LEE, and R. L. Bras, 1991b: Nonlinear Dynamics of
874 Soil-Moisture at Climate Scales .2. Chaotic Analysis. *Water resources Research*, **27**,
875 1907–1915.

876 Romps, D. M., 2011: Response of Tropical Precipitation to Global Warming. *J Atmos Sci*,
877 **68**, 123–138, doi:10.1175/2010JAS3542.1.

878 Rossow, W. B., and R. A. Schiffer, 1999: Advances in understanding clouds from ISCCP.
879 *Bull. Amer. Meteor. Soc*, **80**, 2261–2287.

880 Schlemmer, L., C. Hohenegger, J. Schmidli, C. S. Bretherton, and C. Schaer, 2011: An
881 Idealized Cloud-Resolving Framework for the Study of Midlatitude Diurnal Convection
882 over Land. *J Atmos Sci*, **68**, 1041–1057, doi:10.1175/2010JAS3640.1.

883 Seneviratne, S. I., T. Corti, E. L. Davin, M. Hirschi, E. B. Jaeger, I. Lehner, B. Orlowsky, and
884 A. J. Teuling, 2010: Investigating soil moisture-climate interactions in a changing
885 climate: A review. *Earth-Sci Rev*, **99**, 125–161, doi:10.1016/j.earscirev.2010.02.004.

886 Simpson, J., and V. Wiggert, 1969: Models of Precipitating Cumulus Towers. *Mon Wea*
887 *Rev*, **97**, 471–489.

888 Tompkins, A. M., 2001a: Organization of Tropical Convection in Low Vertical Wind Shears:
889 The Role of Water Vapor. *J Atmos Sci*, **58**, 529–545, doi:10.1175/1520-0469(2001)058.

890 Tompkins, A. M., 2001b: Organization of Tropical Convection in Low Vertical Wind Shears:
891 The Role of Cold Pools. *J Atmos Sci*, **58**, 1650–1672, doi:10.1175/1520-
892 0469(2001)058.

893 Tompkins, A. M., and G. C. Craig, 1998a: Time-scales of adjustment to radiative-convective
894 equilibrium in the tropical atmosphere. *Q J Roy Meteor Soc*, **124**, 2693–2713,
895 doi:10.1002/qj.49712455208.

896 Tompkins, A. M., and G. C. Craig, 1998b: Radiative–convective equilibrium in a three-
897 dimensional cloud-ensemble model. *Q J Roy Meteor Soc*, **124**, 2073–2097,
898 doi:10.1002/qj.49712455013.

899 Wang, G. and Eltahir, E., 2000: Biosphere-atmosphere interactions over West Africa II:
900 Multiple climate equilibria. *Q J Roy Meteor Soc.*, **126**, 1261-1280

901 Wood, R., 2012: Stratocumulus Clouds. *Mon Wea Rev*, **140**, 2373–2423,
902 doi:10.1175/MWR-D-11-00121.1.

Zhang, M., C. S. Bretherton, and P. N. Blossey, 2012: The CGILS experimental design to investigate low cloud feedbacks in general circulation models by using single-column and large-eddy simulation models. *Journal of Advances in Modeling Earth Systems-Discussion*, **4**, doi:10.1029/2012MS000182.

FIGURE CAPTION LIST:

Fig 1: Time-series of a) daily average integrated radiative cooling (blue) and convective heating (red), 10-day running mean b) atmospheric (solid) and soil (dashed) energy budget and c) surface temperature for the CTL run (λ = 35°, Q_{tot} = 40 mm and T_0 = 300 K).

Fig 2: Averaged diurnal cycle over the last three months of a) Surface temperature, b) Precipitation, c) atmosphere (black solid) and soil (black dashed) energy budget (black solid), turbulent fluxes (green), and solar forcing (red), d) vertically integrated convective (red) and radiative (blue) heating decomposed in its short wave (circle line) and long wave (dashed lines) components for the CTL run (λ = 35°, Q_{tot} = 40 mm and T_0 = 300 K).

Fig 3: Average surface temperature T_s (K) versus soil water content Q_{soil} (mm) (Q_{soil} = Q_{tot} - W) over the last three months at different latitudes, for initial soil water content Q_0 = 5 mm (circles), 15 mm (squares), 25 mm (triangles), 35 mm (diamonds) and 45 mm (stars). Grey arrows link the initial state to the final state. The “cool states” (maximum Q_{soil} and minimum T_s) are highlighted in blue, the “warm states” (Q_{soil} ~0 and maximum T_s) in red, and the “intermediate states” in green (0< Q_{soil} < Q_{max} and T_{min} < T_s < T_{max}). The black squares indicate the points families owing to the same equilibrium state (or attractor). Multiple equilibria are present when a group of

arrows originating from the same horizontal line do not converge towards the same attractor. Green symbols that are not squared can correspond to RCE either (1) still not in a steady regime (i.e Net (TOA) different from zero) (2) or may be trapped into an intermediate RCE state that is (i) not shared by any other RCE of this set of experiment (e.g if differences in To are too large between two experiments), or (ii) unique.

Fig 4: Average surface temperature T_s (K) over the last three months at different latitudes, for initial soil water content Q_0 = 5 mm and initial ground temperature T_0 = 280 K (blue), T_0 = 290 K (light blue), T_0 = 300 K (green), T_0 = 310 K (yellow) and T_0 = 320 K (red).

Fig 5: Time series of 10-day running mean a) surface temperature, b) soil water content, c) precipitation, and d) precipitable water for λ = 30° (red), 32.5° (yellow), 35° (green), 37.5° (light blue) and 40° (blue). Initial ground temperature is T_0 =280 K and total water is Q_{tot} =60 mm (i.e. initial Q_0 = 35 mm).

Fig 6: Mean vertical profile over the lasts three months of a) convective (solid) and radiative (dashed) heating, b) relative humidity and c) precipitation for λ = 30° (red), 32.5° (yellow), 35° (green), 37.5° (light blue), 40° (blue). Initial ground temperature is T_0 =280 K and total water is Q_{tot} =60 mm (i.e. initial is Q_0 = 35 mm).

Fig 7: Mean diurnal cycle of the cloud fraction over the last three months at different latitudes. Initial ground temperature is T_0 =280 K and total water is Q_{tot} =60 mm (i.e. initial Q_0 = 35 mm).

Fig 8: Average surface temperature T_s (K) versus soil water content Q_{soil} (mm) (Q_{soil} = Q_{tot} - W) over the last three months a) with fully interactive clouds and b) without cloud

radiative effect, for initial soil water content Q_0 = 5 mm (circles), 15 mm (squares), 25 mm (triangles), 35 mm (diamonds) and 45 mm (stars). Grey arrows link the initial state to the final state. The "cool states" (maximum Q_{soil} and minimum T_s) are highlighted in blue and the "warm states" (Q_{soil} ~0 and maximum T_s) are highlighted in red and "intermediate states" in green ($0< Q_{soil} < Q_{max}$ and $T_{min} < T_s < T_{max}$). The black squares indicate the points families owing to the same equilibrium state (or attractor). Multiple equilibria are present when a group of arrows originating from the same horizontal line do not converge towards the same attractor. Green symbols that are not squared can correspond to RCE either (1) still not in a steady regime (i.e. Net TOA different from zero) (2) or may be trapped into an intermediate RCE state that is (i) not shared by any other RCE of this set of experiment (e.g. if differences in T_0 are too large between two experiments), or (ii) unique. Latitude is prescribed at 35°.

Fig 9: Time series of 10-day running mean surface temperature for λ = 30° (red), 32.5° (yellow), 35° (green), 37.5° (light blue) and 40° (blue) with a) fully interactive clouds, b) without cloud radiative effect, c) only with low clouds (P < 600 hPa) radiative effect, and d) only high clouds (P > 600 hPa) radiative effect. Initial ground temperature is T_0 =280 K and total water is Q_{tot} =60 mm (i.e. initial is Q_0 = 25 mm).

Fig 10: Same as Fig 8 with a wind forcing nudged towards a geostrophic value of 10 m/s.

974

975

976

977

Figures

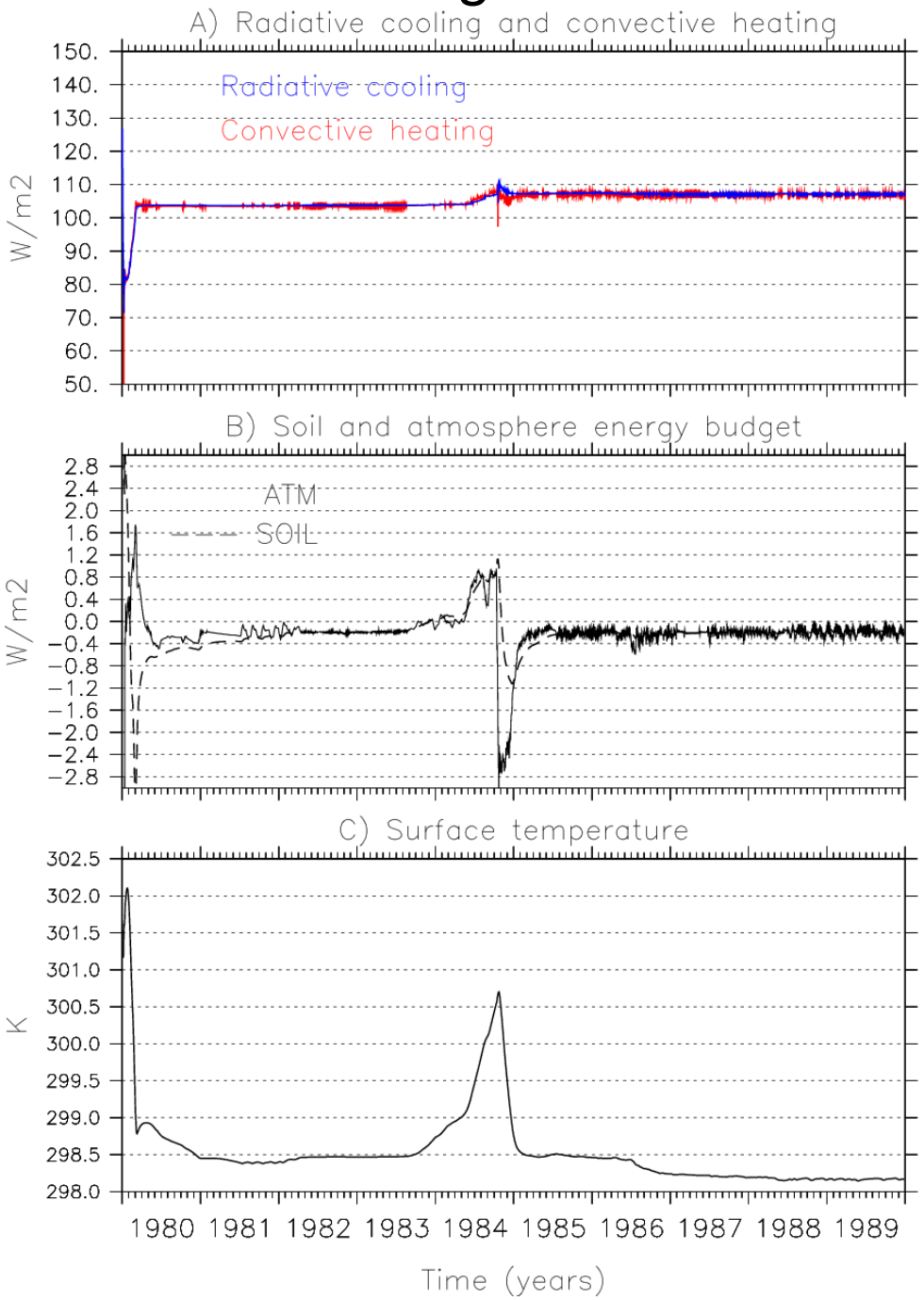

Fig 1: Time-series of a) daily average integrated radiative cooling (blue) and convective heating (red), 10-day running mean b) atmospheric (solid) and soil (dashed) energy budget and c) surface temperature for the CTL run (λ = 35°, Q_{tot} = 40 mm and T_0 = 300 K).

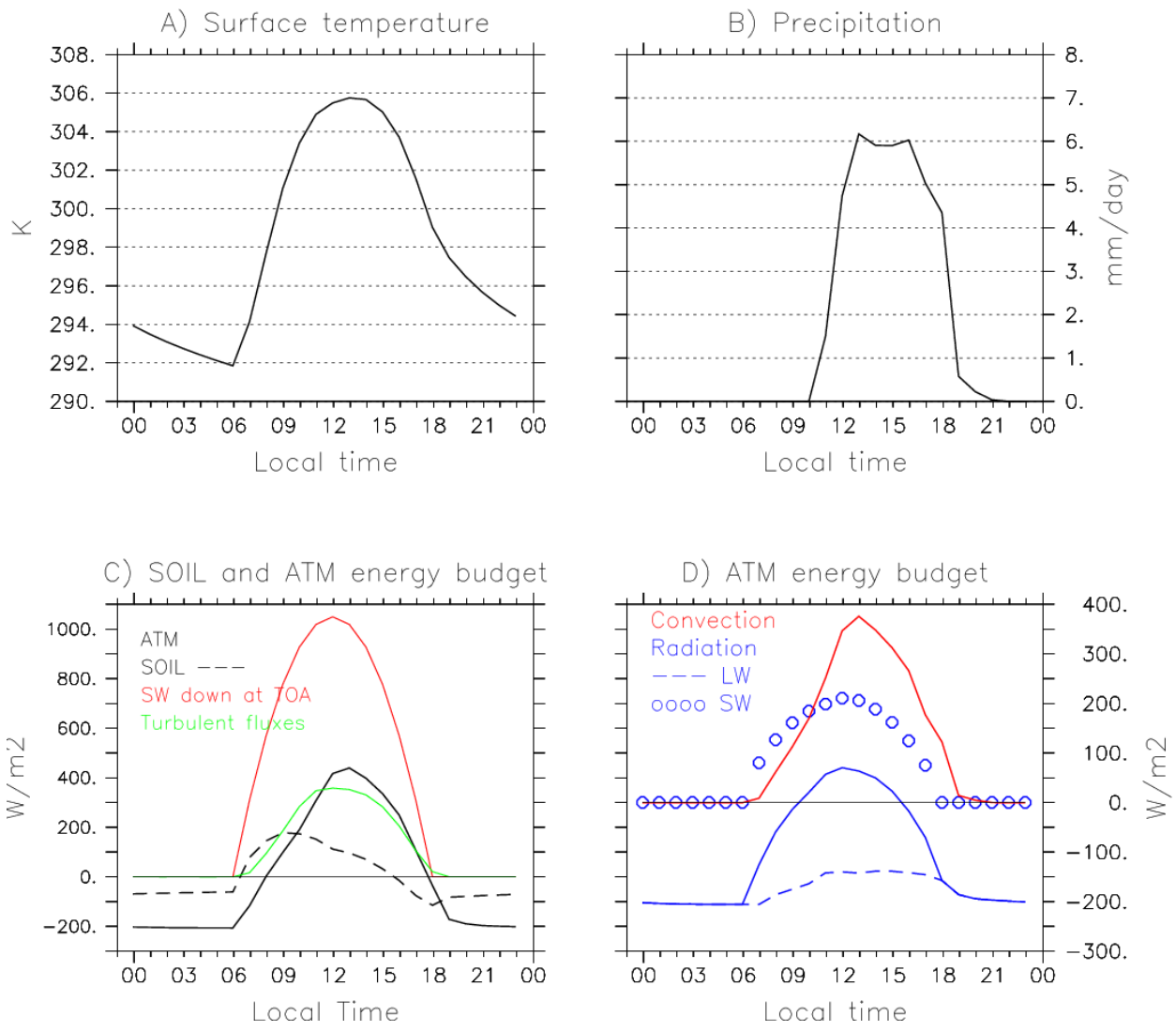

Fig 2: Averaged diurnal cycle over the last three months of a) Surface temperature, b) Precipitation, c) atmosphere (black solid) and soil (black dashed) energy budget (black solid), turbulent fluxes (green), and solar forcing (red), d) vertically integrated convective (red) and radiative (blue) heating decomposed in its short wave (circle line) and long wave (dashed lines) components for the CTL run (λ = 35°, Q_{tot} = 40 mm and T_0 = 300 K).

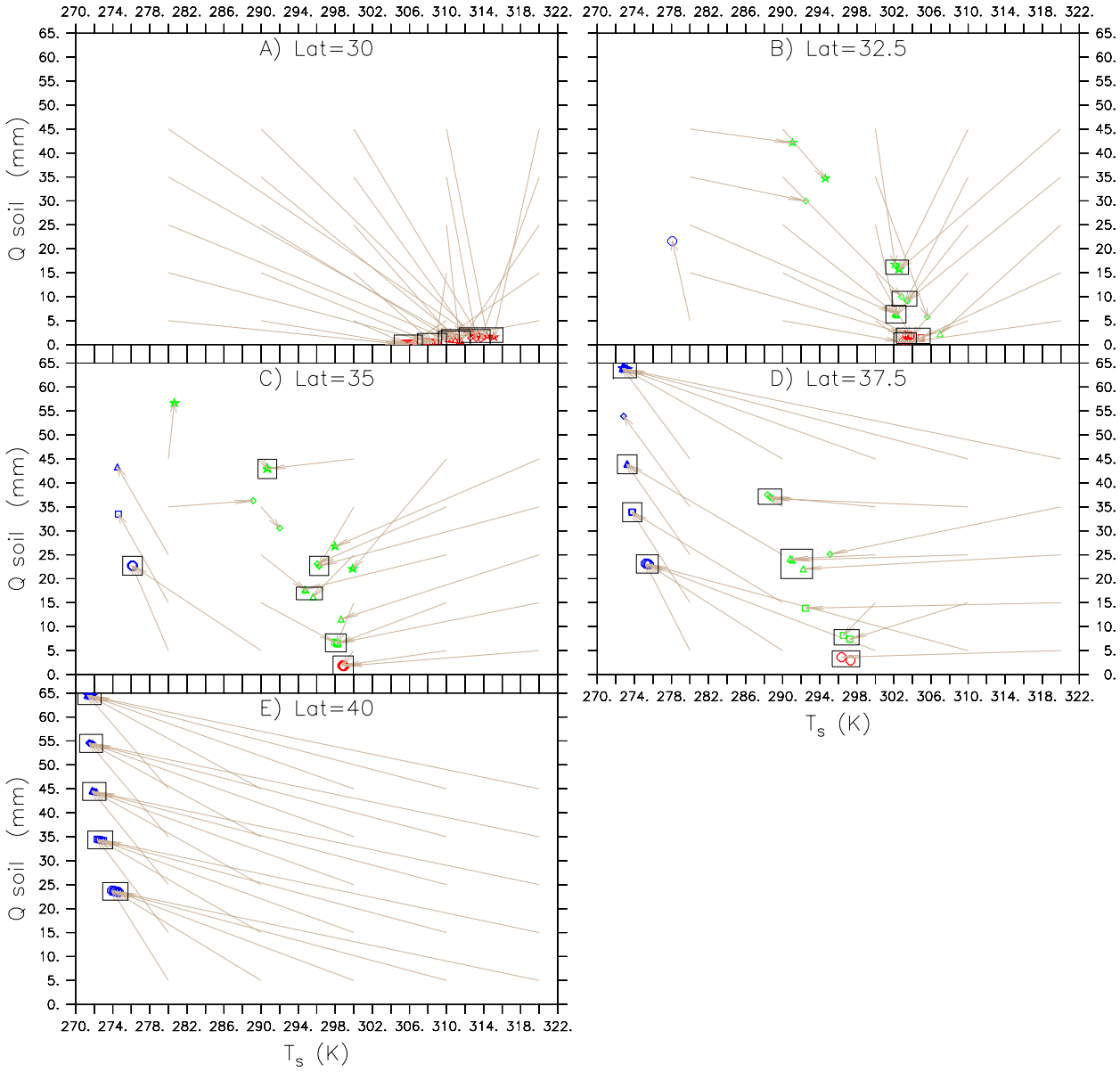

994

995 Fig 3: Average surface temperature T_s (K) versus soil water content Q_{soil} (mm) (Q_{soil} = Q_{tot} -
996 W) over the last three months at different latitudes, for initial soil water content Q_0 = 5
997 mm (circles), 15 mm (squares), 25 mm (triangles), 35 mm (diamonds) and 45 mm
998 (stars). Grey arrows link the initial state to the final state. The “cool states” (maximum
999 Q_{soil} and minimum T_s) are highlighted in blue, the “warm states” (Q_{soil} ~0 and
1000 maximum T_s) in red, and the “intermediate states” in green (0< Q_{soil} < Q_{max} and T_{min} <
1001 T_s < T_{max}). The black squares indicate the points families owing to the same

equilibrium state (or attractor). Multiple equilibria are present when a group of arrows originating from the same horizontal line do not converge towards the same attractor. Green symbols that are not squared can correspond to RCE either (1) still not in a steady regime (i.e Net (TOA) different from zero) (2) or may be trapped into an intermediate RCE state that is (i) not shared by any other RCE of this set of experiment (e.g if differences in To are too large between two experiments), or (ii) unique.

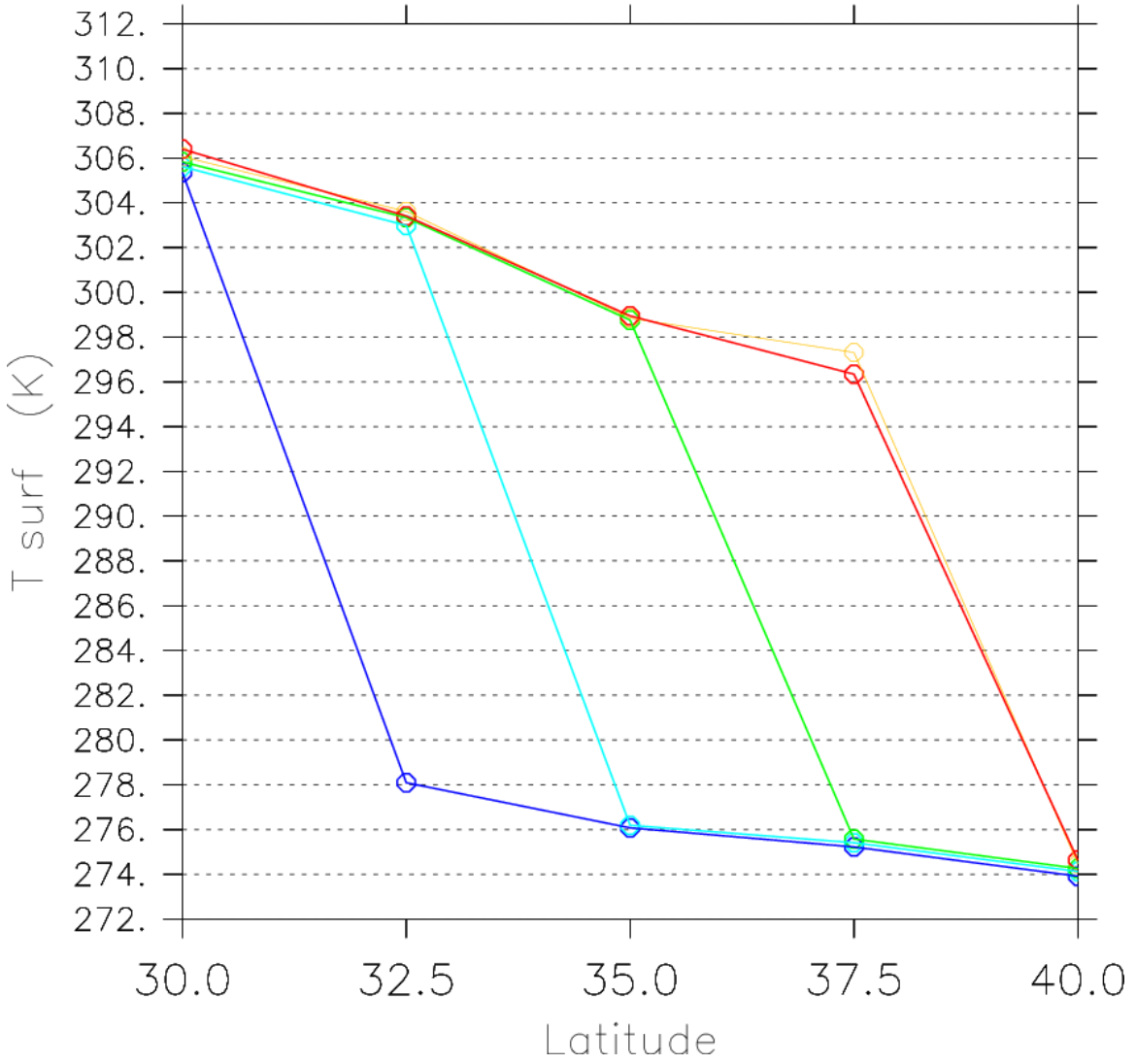

Fig 4: Average surface temperature T_s (K) over the last three months at different latitudes, for initial soil water content Q_0 = 5 mm and initial ground temperature T_0 = 280 K (blue), T_0 = 290 K (light blue), T_0 = 300 K (green), T_0 = 310 K (yellow) and T_0 = 320 K (red).

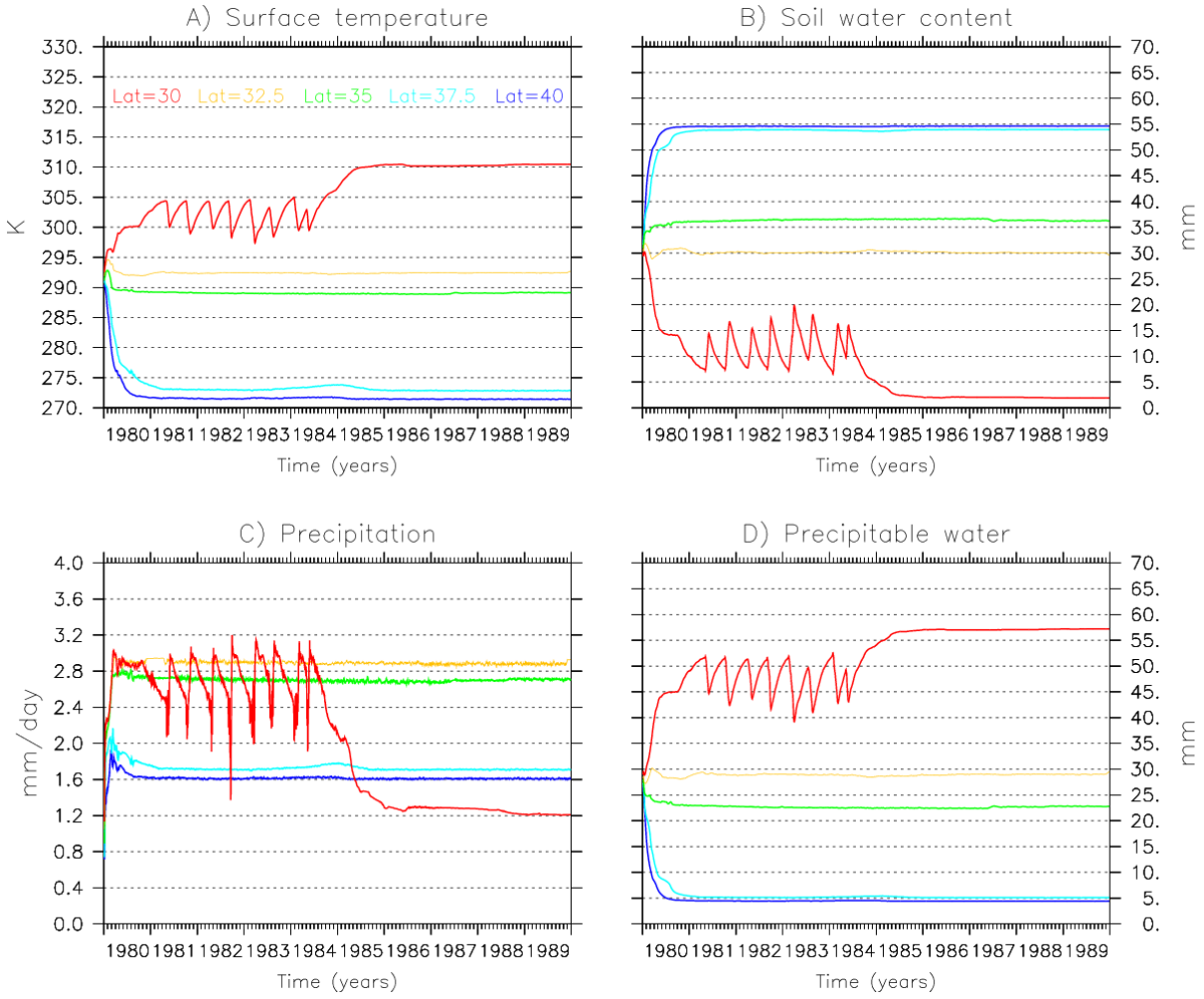

Fig 5: Time series of 10-day running mean a) surface temperature, b) soil water content, c) precipitation, and d) precipitable water for λ = 30° (red), 32.5° (yellow), 35° (green), 37.5° (light blue) and 40° (blue). Initial ground temperature is T_0 =280 K and total water is Q_{tot} =60 mm (i.e. initial Q_0 = 35 mm).

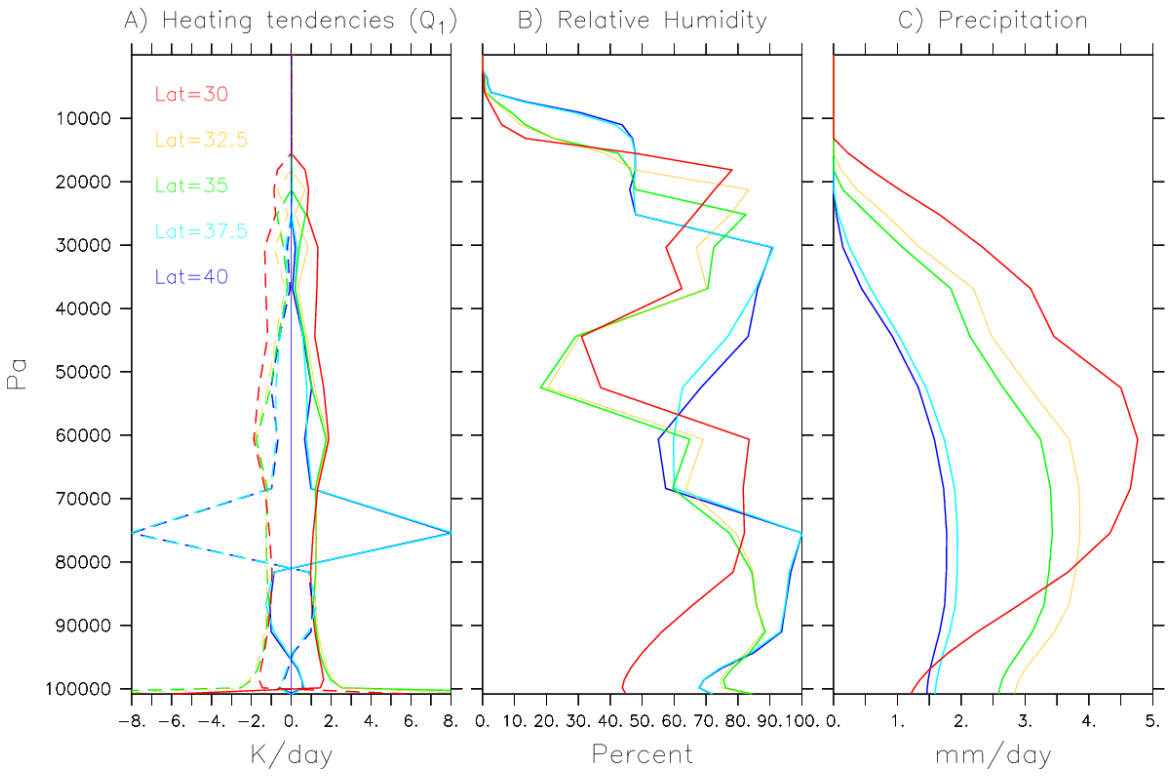

Fig 6: Mean vertical profile over the lasts three months of a) convective (solid) and radiative (dashed) heating, b) relative humidity and c) precipitation for λ = 30° (red), 32.5° (yellow), 35° (green), 37.5° (light blue), 40° (blue). Initial ground temperature is T_0 =280 K and total water is Q_{tot} =60 mm (i.e. initial is Q_0 = 35 mm).

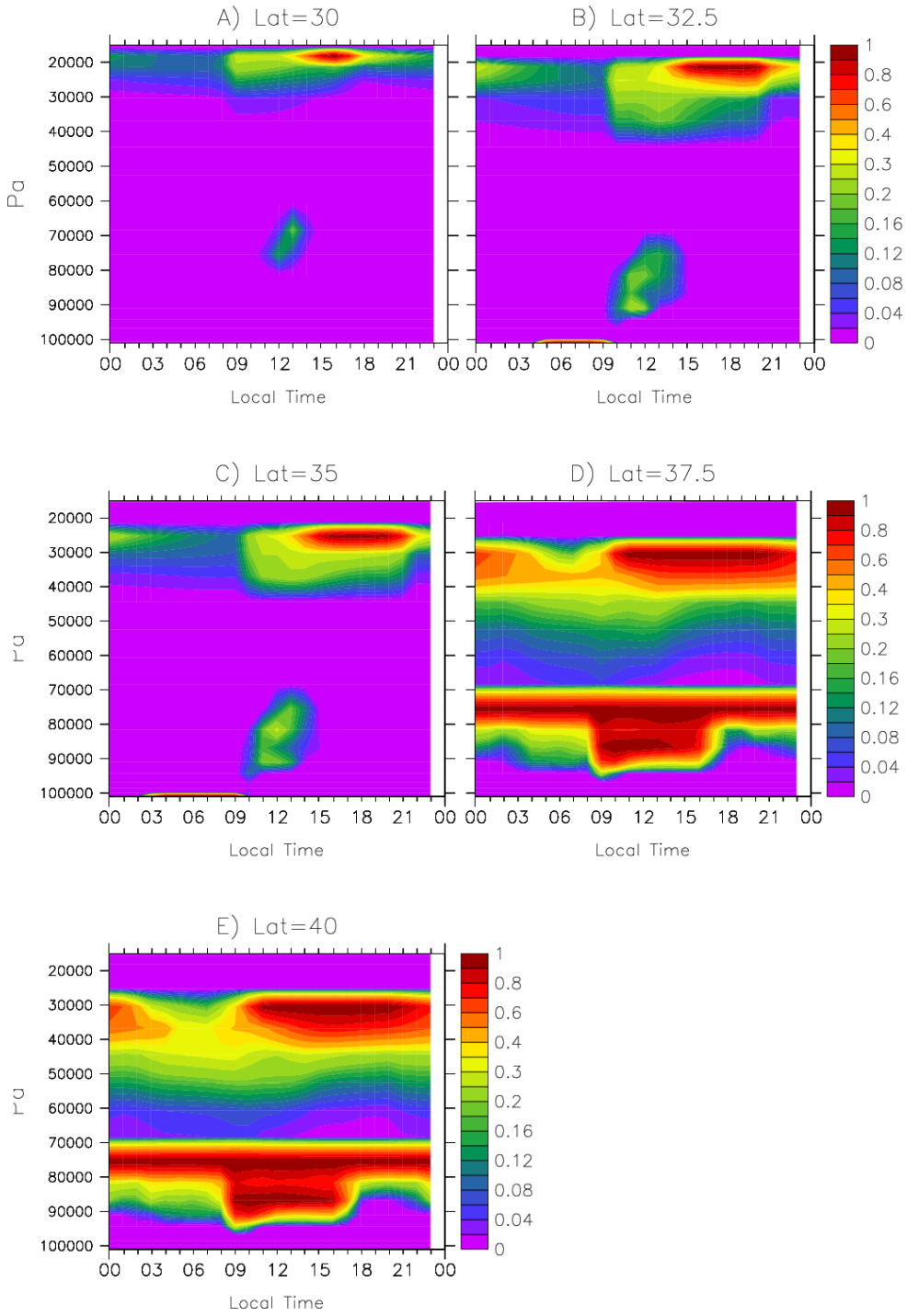

Fig 7: Mean diurnal cycle of the cloud fraction over the last three months at different latitudes. Initial ground temperature is T_0 =280 K and total water is Q_{tot} =60 mm (i.e. initial Q_0 = 35 mm).

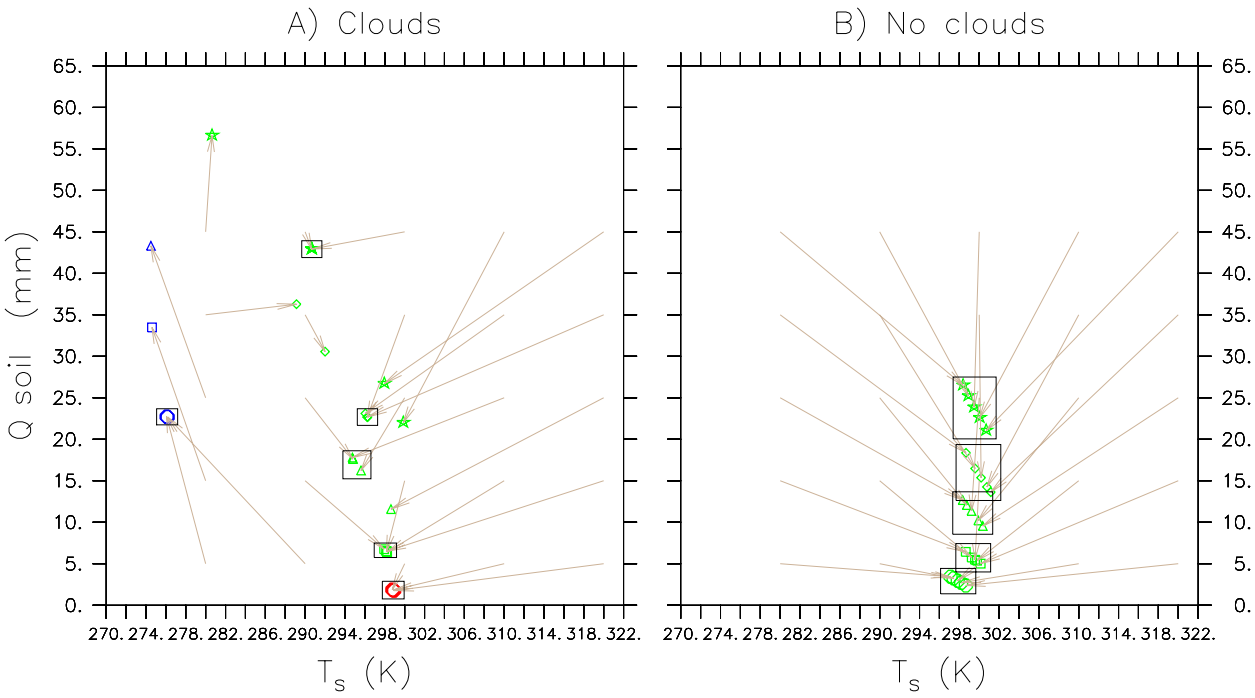

Fig 8: Average surface temperature T_s (K) versus soil water content Q_{soil} (mm) (Q_{soil} = Q_{tot} - W) over the last three months a) with fully interactive clouds and b) without cloud radiative effect, for initial soil water content Q_0 = 5 mm (circles), 15 mm (squares), 25 mm (triangles), 35 mm (diamonds) and 45 mm (stars). Grey arrows link the initial state to the final state. The "cool states" (maximum Q_{soil} and minimum T_s) are highlighted in blue and the "warm states" (Q_{soil} ~0 and maximum T_s) are highlighted in red and "intermediate states" in green (0< Q_{soil} < Q_{max} and T_{min} < T_s < T_{max}). The black squares indicate the points families owing to the same equilibrium state (or attractor). Multiple equilibria are present when a group of arrows originating from the same horizontal line do not converge towards the same attractor. Green symbols that are not squared can correspond to RCE either (1) still not in a steady regime (i.e. Net TOA different from zero) (2) or may be trapped into an intermediate RCE state that is (i) not shared by any other RCE of this set of experiment (e.g. if differences in T_0 are too large between two experiments), or (ii) unique. Latitude is prescribed at 35°.

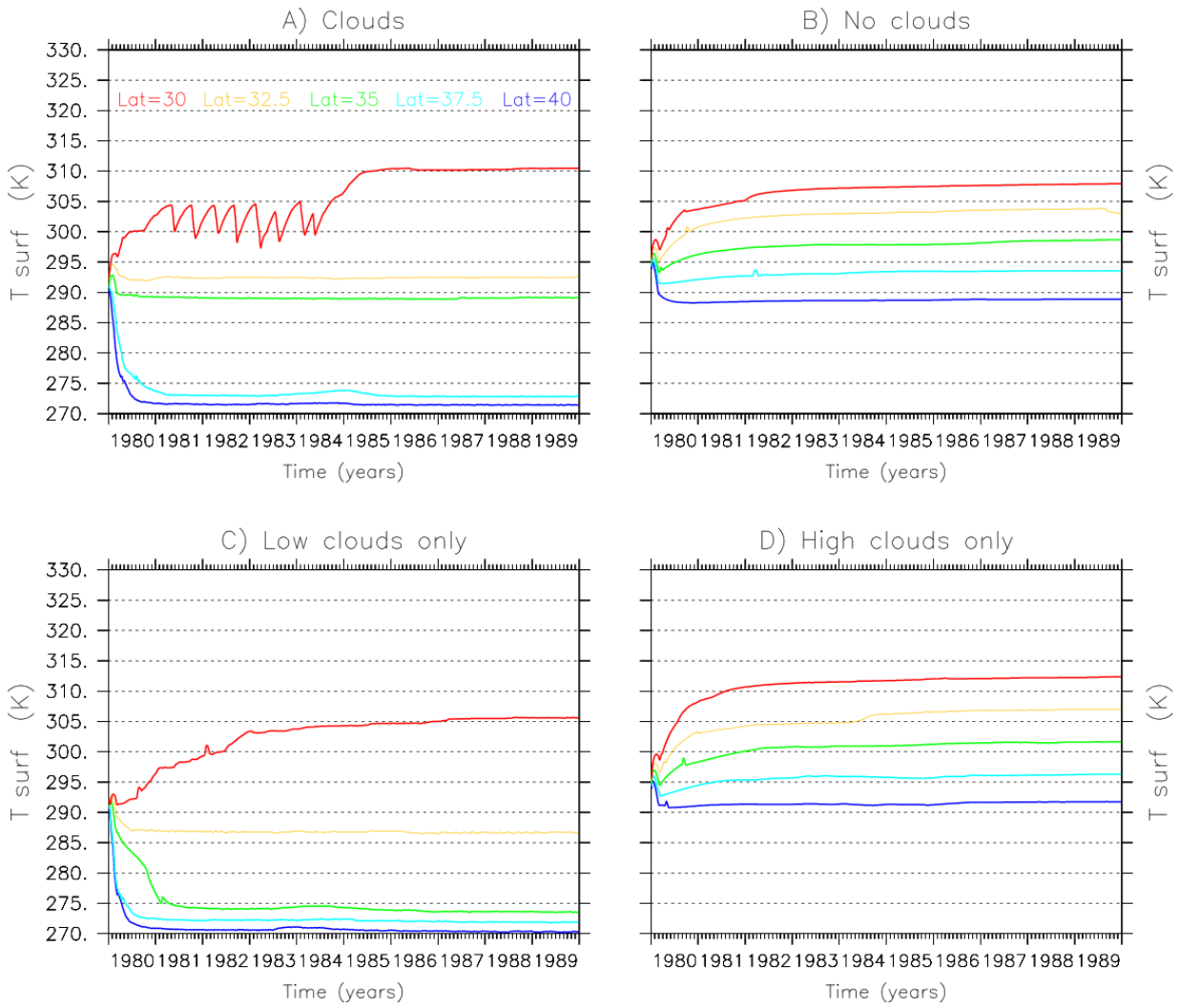

Fig 9: Time series of 10-day running mean surface temperature for λ = 30° (red), 32.5° (yellow), 35° (green), 37.5° (light blue) and 40° (blue) with a) fully interactive clouds, b) without cloud radiative effect, c) only with low clouds (P < 600 hPa) radiative effect, and d) only high clouds (P > 600 hPa) radiative effect. Initial ground temperature is T_0 =280 K and total water is Q_{tot} =60 mm (i.e. initial is Q_0 = 25 mm).

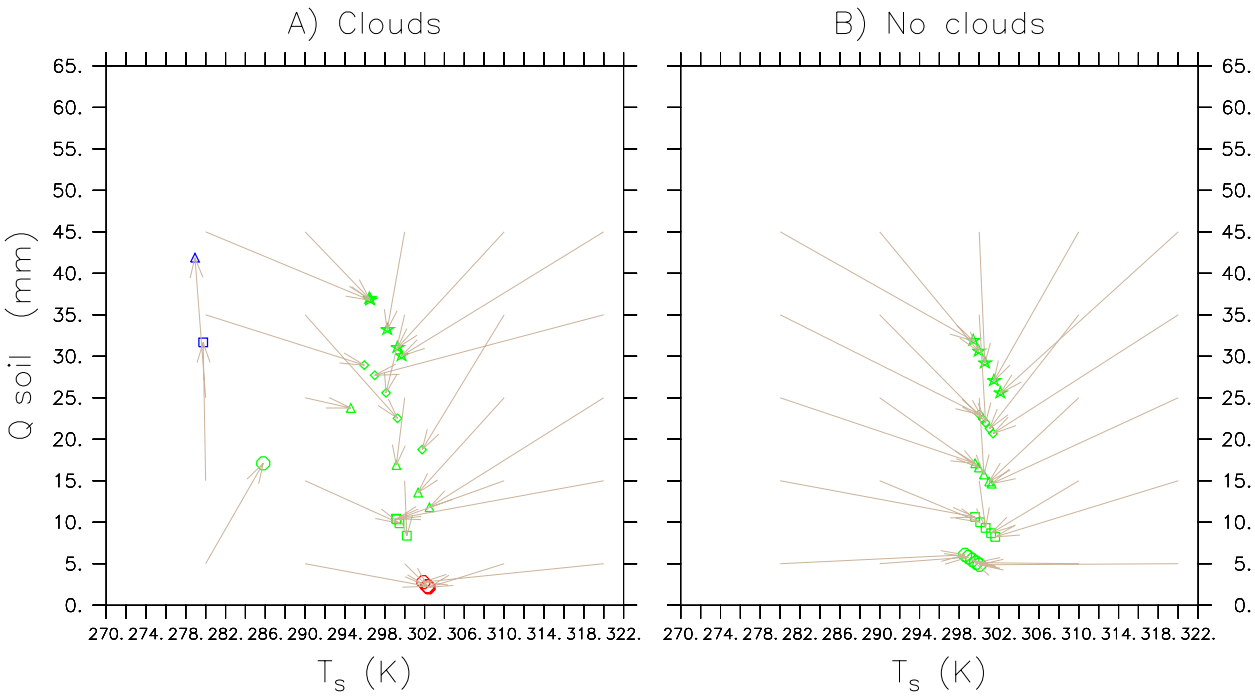

1075

1076 Fig 10: Same as Fig 8 with a wind forcing nudged towards a geostrophic value of 10 m/s.

1077

1078